AGU PUBLICATIONS

Radio Science

RESEARCH ARTICLE
10.1002/2016RS006165

Key Points:
- Statistics of scintillation and loss of lock
- Relationship between amplitude and phase scintillation
- Frequency dependence of scintillation

Correspondence to:
A. O. Moraes,
alisonaom@iae.cta.br

Citation:
Moraes, A. O., E. Costa, M. A. Abdu, F. S. Rodrigues, E. R. de Paula, K. Oliveira, and W. J. Perrella (2017), The variability of low-latitude ionospheric amplitude and phase scintillation detected by a triple-frequency GPS receiver, *Radio Sci.*, *52*, 439–460, doi:10.1002/2016RS006165.

Received 2 SEP 2016
Accepted 18 MAR 2017
Accepted article online 24 MAR 2017
Published online 10 APR 2017

The variability of low-latitude ionospheric amplitude and phase scintillation detected by a triple-frequency GPS receiver

Alison de Oliveira Moraes[1], Emanoel Costa[2], Mangalathayil Ali Abdu[3,4], Fabiano S. Rodrigues[5], Eurico Rodrigues de Paula[3], Kelias Oliveira[6], and Waldecir João Perrella[4]

[1]Instituto de Aeronáutica e Espaço, São José dos Campos, Brazil, [2]Centro de Estudos em Telecomunicações, Pontifícia Universidade Católica do Rio de Janeiro, Rio de Janeiro, Brazil, [3]Instituto Nacional de Pesquisas Espaciais, São José dos Campos, Brazil, [4]Instituto Tecnológico da Aeronáutica, São José dos Campos, Brazil, [5]William B. Hanson Center for Space Sciences, University of Texas at Dallas, Richardson, Texas, USA, [6]Instituto Federal de Educação, Ciência e Tecnologia de Goiás, Goiânia, Brazil

Abstract Ionospheric scintillation is a manifestation of space weather effects that seriously affect the performance and availability of space-based navigation and communication systems. This paper presents results from an investigation on the characteristics of the phase and amplitude scintillation of Global Positioning System signals at the L1, L2C, and L5 frequencies. Field data obtained by a scintillation monitor installed in São José dos Campos (23.1°S, 45.8°W; dip latitude 17.3°S, declination 21.4°W), Brazil, a station located near the southern crest of the equatorial ionization anomaly, were used for this purpose. The analyzed data were collected during 150 nights from November 2014 to March 2015, an epoch of moderate solar activity close to the recent solar maximum. Only measurements corresponding to an elevation mask of 30° and values above standard threshold levels were used in the analysis. Outstanding characteristics of amplitude and phase scintillation are analyzed and compared in this study. The different characteristics of the scintillation focused in this study include (1) the statistics of their occurrences at the three frequencies; (2) the local time distributions of the amplitude and phase scintillation at different intensity levels; (3) azimuth-elevation (spatial) distributions at different levels of the standard deviation of phase fluctuations; (4) scintillation enhancement and loss of phase lock conditions due to field-aligned (longitudinal) propagation; (5) the relationship between amplitude and phase scintillation parameters for the L1, L2C, and L5 frequencies; and (6) the frequency dependence of the amplitude and phase scintillations. Important results on these different characteristics are presented and discussed, and some outstanding problems for future investigations are suggested.

1. Introduction

The structuring and dynamics of the nighttime ionosphere that characterize the equatorial spread *F* (ESF) irregularity phenomenon can cause severe deteriorating impacts on satellite radio signals received at the ground. The ESF irregularities develop in the postsunset equatorial ionosphere through plasma interchange instability processes driven by the Rayleigh-Taylor (R-T) mechanism that initiates at the bottomside gradient region of a rapidly rising evening *F* layer. The nonlinear growth of the instability involves the lower density plasma rising up to the topside ionosphere in the form of plasma-depleted flux tubes (magnetic field-aligned plasma bubbles, equatorial plasma bubble (EPB)), with extremities extending to latitudes of larger background plasma density in the equatorial ionization anomaly. As a result of the vertical growth of the plasma-depleted magnetic flux tubes characterizing a typical bubble development process, irregularities are observed, in the hours immediately following the sunset, first over dip equatorial regions followed by their later occurrence with increasing time delay at off-equatorial latitudes. During their evolution, the EPBs generally drift eastward. Secondary instabilities develop at the steepening gradient regions of the rising bubbles in a cascading process leading to hierarchy of irregularities with decreasing scale sizes [*Haerendel*, 1973]. However, diffusive losses dominate the R-T instability growth and the cascading process at short-scale sizes (a few hundreds to several tens of meters) [*Kelley et al*., 2011], which may explain the different slopes observed in the power spectral densities of the irregularities over a range from a few hundred kilometers to a few meters [*Rodrigues et al*., 2009].

Motions of medium-scale density structures across transionospheric raypaths form moving complex field patterns at the ground that include amplitude and phase structures. Thus, random temporal fluctuations

are produced in both amplitude and phase of satellite signals received at the ground. These fluctuations are known as amplitude and phase scintillation, respectively [*Yeh and Liu*, 1982; *Kintner et al*., 2004; *Kintner et al*., 2007]. Assuming a phase screen at the altitude $z = 350$ km, the Fresnel scale sizes $(\lambda z)^{1/2}$ at the L1, L2C, and L5 frequencies would be approximately equal to 460 m, 520 m, and 530 m, respectively. It is commonly accepted that irregularities with scale sizes less than these are generally responsible for scintillation of transionospheric signals emitted by the Global Positioning System (GPS) satellites through the diffractive scattering mechanism. Under geomagnetically quiet conditions, the equatorial scintillation activity develops in the postsunset hours and typically lasts for 4–5 h until midnight, sometimes also extending for a few hours into the postmidnight period. It presents strong seasonal and longitudinal variations that depend on the alignment of the sunset terminator with the magnetic meridian [*Abdu et al*., 1981; *Tsunoda*, 1985]. They additionally depend on other factors related to seasonal variations in the thermospheric winds and instability-seeding sources, such as gravity waves. In the Brazilian region, scintillation activity extends from September to March and peaks in the southern summer months. In addition, scintillation undergoes significant short-term variability due to geophysical drivers, such as upward propagating atmospheric waves, sudden stratospheric warming episodes, and changes in solar and magnetic activities [*Aarons*, 1982; *Basu et al*., 2001; *de Paula et al*., 2015].

Scintillation may be responsible for significant degradation in the operational accuracy of Global Positioning System (GPS) receivers. As pointed out by several authors [*Skone et al*., 2001; *Doherty et al*., 2003; *Zou and Wang*, 2009], rapid phase variations can produce cycle slips. In extreme cases, depending on the processor performance, they may challenge the receiver ability to hold phase lock. Additionally, amplitude fades can cause the signal-to-noise ratio to drop below receiver threshold. These effects may increase the range measurement errors or may even cause the carrier and code loops to lose lock [*Kintner et al*., 2001]. Depending on its severity, scintillation can result in full disruption of the receiver operation or may lead to complete system failures [*Basu and Basu*, 1981; *Beach*, 1998; *de Rezende et al*., 2007]. Such extreme phenomena are more usual near the equatorial and low-latitude regions (between approximately $-20°$ and $+20°$ geomagnetic latitude) than in the auroral and polar zones (above 55° of latitude). It should be noted that *Dao et al*. [2012] applied a zero-order approximation to their sophisticated model of the distribution of ion density depletions along magnetic field lines. The approximation indicates that ion density perturbations (with strength of the irregularities ΔN) remain proportional to the ambient density along these field lines. Since the intensity of scintillation increases with the strength of irregularity structures, both generally accompany the background plasma density [*Aarons*, 1982]. This explains why the occurrence of more intense scintillation is greater at the crest of equatorial anomaly region (around approximately $\pm 15°$), where the background plasma density is higher, than that at the ionization trough around the dip equator, as experimentally observed by *Basu et al*. [1988] and *de Paula et al*. [2003].

In view of such detrimental/disruptive effects of scintillation on different space application systems related to navigation and telecommunications, and especially on the operability of the Global Navigation Satellite Systems (GNSS) receivers, it is very important to investigate their statistical characteristics. Based on such continued efforts, techniques can be developed to mitigate the identified degrading effects and improve the robustness of GNSS receivers under ionospheric scintillation.

Scintillation occurs dominantly at equatorial, low-, and high-latitude regions of the Earth. In this context, some pertinent statements by *Aquino and Sreeja* [2013] should be quoted: "At GNSS frequencies, amplitude scintillation is not of significant concern for auroral and polar latitudes. Phase scintillation however poses a greater concern. Phase scintillation induces rapid phase shifts, which may exceed the phase-locked loop (PLL) bandwidth, resulting in loss of phase lock." The morphology of phase scintillation in the auroral oval and polar cap was well established by *Basu et al*. [1985]. Recently, several works with analyses of phase scintillation have been reported for different high-latitude sites [*Li et al*., 2010; *Prikryl et al*., 2011a; *Prikryl et al*., 2011b; *Jiao et al*., 2013; *Prikryl et al*., 2014; *Sreeja and Aquino*, 2014]. On the other hand, amplitude scintillation is very important at equatorial and low latitudes and dominates over the effects of phase scintillation. However, as explained in the third paragraph, the effects of phase scintillation should not be ignored in these regions. Indeed, in the model proposed by *Conker et al*. [2003] to estimate the effects of scintillation on the performance of GPS receivers, the variance of the tracking error at the output of the PLL is a sum of three components, due to phase scintillation, thermal noise (amplitude scintillation), and oscillator noise. Furthermore, *Sreeja et al*. [2011] have shown in their Figure 6b that the contributions of the first two

components are equivalent. Their results are supported by those from simulations by *Skone et al*. [2005]. Further, the results to be presented here will show clearly good correspondence between the scintillation features as diagnosed by both the amplitude and phase measurements of the GNSS signals, which opens up the possibility of using phase scintillation measurements as a valuable tool complementary to that of the amplitude scintillation in the investigation of the ionospheric irregularities at low latitude.

Measurement of phase scintillation has additional utility for the diagnostics of the low-latitude ionosphere. For example, *Carrano et al*. [2016] recently proposed a procedure to estimate the zonal irregularity drift from single-station GNSS measurements of S_4 and σ_{φ}, to be used when the well-established spaced-receiver measurements are not possible. It is based on the weak scatter scintillation theory, considering the propagation geometry. The procedure also requires assumptions on the height of the scattering layer and the spectral index of the power spectral density of the irregularities. They validated the technique by using VHF spaced-receiver measurements of the zonal irregularity drift. Particularly, in the equatorial region, it appears that intensity scintillation is the main driver of PLL problems [*Van Dierendonck*, 2008]. Indeed, some PLL designs may even suppress phase scintillation, which would impair the use of such a receiver as a diagnostic tool. Thus, it evident from the present and the previous paragraphs that the processor response to strong scintillation remains a research issue. It should also be noted that the approach proposed by *Carrano et al*. [2016] will not be explored in the present paper.

Aligned with the above understanding on the relevance of phase scintillation studies at equatorial and low latitudes, corresponding measurements have been performed in the Asian sector [*Gwal et al*., 2006; *Xu et al*., 2012; *Forte*, 2012]. Additionally, *Doherty et al*. [2003] and *Jiao and Morton* [2015] compared results from scintillation measurements performed in Peru and at high-latitude sites. The latter authors also reported on experimental results from Ascension Island. It is well known that the morphology of ionospheric irregularities at equatorial and low latitudes are highly dependent on the longitude sector [*Huang et al*., 2014; *Costa et al*., 2014], that the Brazilian sector displays one of the global maxima in their occurrence rates [*Kil et al*., 2006; *Su et al*., 2008], and that a similar dependence is extended to scintillation [*Basu and Basu*, 1981]. L-band amplitude scintillation has been extensively studied over the Brazilian sector [*de Paula et al*., 2003; *de Rezende et al*., 2007; *Muella et al*., 2008; *Moraes et al*., 2012], but corresponding phase scintillation information is missing. The purpose of the present paper is to fill this gap by investigating and statistically characterizing the standard deviation of phase scintillation over a low-latitude region in the Brazilian sector. The results will be compared with the relevant/related description of the parameter for amplitude scintillation simultaneously measured in the Brazilian sector, in an effort to evaluate the conditions of their potential impact on GNSS applications. The conditions affecting the scintillation intensity due to the signal propagation path aligning with geomagnetic field-aligned plasma bubbles will also be discussed.

The paper is organized in the following way. Section 2 describes the experimental setup, the period of analysis, and the geophysical condition during measurements. Section 3 introduces the observed values for the standard deviation of the phase fluctuations in the received signals at the three available GPS frequencies. It indicates the typical values and the frequency of occurrences that a user may expect under similar circumstances. Section 4 discusses the spatial distribution of the scintillation events, enhancing the current understanding on how the irregularities affect users of GNSS systems in low-latitude regions. Section 5 analyzes the relation between the amplitude and phase scintillation parameters, showing how they relate under different scattering conditions. Section 6 presents the relation among scintillation parameters for the three GPS frequencies, verifying the validity of widely used frequency-scaling expressions [*Fremouw et al*., 1978; *Yeh and Liu*, 1982]. Finally, section 7 summarizes the study and presents concluding remarks.

2. Measurements, Data Processing, and Initial Analysis

The experimental data utilized in this study were measured by one of the PolaRxS triple-frequency (L1, L2C, and L5) receivers with ultralow-noise Oven-Controlled Crystal Oscillators of the Concept for Ionospheric Scintillation Mitigation for Professional GNSS in Latin America/Countering GNSS high Accuracy applications Limitations due to Ionospheric disturbances in Brazil (CIGALA/CALIBRA) network [*Vani et al*., 2016]. The receiver was operated at São José dos Campos (SJC), Brazil, (23.21°S, 45.95°W, −17.5° dip latitude, declination 21.4°W), a site near the southern crest of the equatorial anomaly. This is a region known for the occurrence of strong amplitude scintillation, but with limited studies on phase scintillation events.

The analysis was limited to postsunset up to early postmidnight hours (19:00 LT to 02:00 LT) during the period between 01 November 2014 and 30 March 2015, which is part of the strong and frequent scintillation occurrence season associated with equatorial spread *F* phenomenon observed in the Brazilian longitude sector [*Abdu et al*., 1992; *Sobral et al*., 2002; *de Rezende et al*., 2007]. Data were actually recorded during 140 days out of the total of 150 days. During this 5 month period, the monthly mean absolute values of the 10.7 cm solar radio flux ($F_{10.7}$) were respectively 155.2 solar flux unit (sfu), 158.7 sfu, 141.7 sfu, 128.8 sfu, and 126.0 sfu, where $1\ \text{sfu} = 10^{-22}\ \text{W m}^{-2}\ \text{Hz}^{-1}$. Data for all levels of geomagnetic activity were considered in the analysis.

The parameters used in this analysis are the amplitude and phase scintillation indices S_4 and σ_φ calculated from measurements performed at the three GPS frequencies L1 (1575.42 MHz), L2C (1227.60 MHz), and L5 (1176.45 MHz). The indices σ_φ and S_4 are the standard deviations of δ_φ and $I/\langle I\rangle$ [*Van Dierendonck et al*., 1993], respectively, where δ_φ is the unwrapped and detrended carrier phase (using a sixth-order Butterworth high-pass filter with the default cutoff frequency of 0.10 Hz), *I* is the detrended signal intensity, and $\langle I\rangle$ represents its average value during the computational interval. The receiver automatically samples δ_φ and *I* at 50 Hz and computes both indices every 60 s using the preceding 3000 points for all tracked satellites and at the three frequencies. The values of S_4 are also corrected to eliminate the thermal noise contribution. Using similar procedures, the receiver records $\sigma_{\varphi xx}$ indices for xx = 01, 03, 10, and 30, which are the average of the (60/xx) standard deviations computed over consecutive and nonoverlapping *xx*-s intervals during the last minute. Note that σ_φ is equal to $\sigma_{\varphi 60}$. For each frequency, a signal counter accumulates the number of seconds since the last lock time.

Note that the TEC measurement capability by the receiver was used to control the quality of the scintillation data analyzed here, as described below. At every minute, the receiver also provides the last four total electron content (TEC) values measured at the current time of the week (TOW, s), at TOW-15, TOW-30, and TOW-45, with basis on the L2-P and L1-P pseudoranges. Additionally, differential TEC (dTEC) values, computed from carrier phase measurements only, report the TEC changes between the four consecutive 15 s intervals during the last minute. Similarly, another counter accumulates the number of seconds since the last lock time on the second frequency used for the TEC computation.

To be accepted, a 1 min record should contain the S_4, σ_φ, all $\sigma_{\varphi xx}$ (for any xx) values and the signal counter should be greater than 60 s, for the particular frequency. For the three frequencies, all the TEC or dTEC values should be present and the TEC counter should also be greater than 60 s. Note that the TEC counter and TEC and dTEC values were in fact the two most important sources of data rejection. In addition, an elevation mask of 30° was always used to minimize multipath and nonionospheric effects on the received signal. All recorded samples that met the above criteria during the previously mentioned 5 months were used in the analysis.

In the presence of combinations of GPS satellites and their own motions, plasma irregularities drift across raypaths with a velocity of about 150 m/s. Thus, 500 m irregularities that cause scintillation at GPS frequencies would not be well represented in 01 s or 03 s records (corresponding to the scale-size limit of 450 m), indicating that $\sigma_{\varphi 01}$ or even $\sigma_{\varphi 03}$ would not be adequate for the present study. Additionally, comparisons based on all the data set selected using the criteria of the previous paragraph indicated an almost functional relationship $\sigma_{\varphi 10} \approx \sigma_{\varphi 30} \approx \sigma_{\varphi 60} = \sigma_\varphi$ between the involved indices. On the other hand, it should be remarked that rate of TEC index (ROTI), which is the standard deviation of ROT evaluated at every 5 min, has also been used as an indicator of fluctuations in the received signal. ROT is the rate of change of TEC over 30 s intervals [*Pi et al*., 1997; *Zou and Wang*, 2009]. However, as discussed by the latter authors, ROTI is sensitive to 6 km irregularities, much larger than the Fresnel scale sizes of interest. The above arguments justify the selection of $\sigma_\varphi = \sigma_{\varphi 60}$ as the only indicator of phase scintillation in the present work, in alignment with several other authors [*Doherty et al*., 2003; *Zou and Wang*, 2009; *Sreeja et al*., 2011].

Before presenting and discussing the results from the present experimental campaign, several problems with data treatment and scintillation indices should be acknowledged [*Forte and Radicella*, 2002; *Beach*, 2006; *Moraes et al*., 2014]. However, it should be observed that the above Ionospheric Scintillation Monitor (ISM) and the applied preprocessing of the raw data meet the recommendations by respected developers [*Van Dierendonck et al*., 1993; *Van Dierendonck*, 2008], being also aligned with the conventional practice [*Doherty et al*., 2003; *Jiao and Morton*, 2015]. In addition, the S_4 and σ_φ indices are undoubtedly the most widely adopted parameters in the description of ionospheric scintillation and will be used here to maintain consistency with the bulk of the associated literature.

Table 1. Data Availability and Number of Samples for Different Thresholds and Local Time Intervals

	19:00 LT–01:59 LT			20:00 LT–22:59 LT			20:00 LT–21:59 LT		
Number of Samples	L1	L2C	L5	L1	L2C	L5	L1	L2C	L5
Total	307,596	109,790	65,575	12,5091	41,824	22,616	81,901	28,288	13,953
$S_4 > 0.3$	21,214	9,370	6,187	14,186	5,559	3,303	8,234	3,301	1,836
$S_4 > 0.7$	3,076	1,879	1,767	2,383	1,402	1,259	1,582	969	867
$S_4 > 1.0$	383	286	371	311	212	274	192	155	189
$\sigma_\varphi > 10°$	17,018	6,348	3,895	12,153	4,220	2,534	7,012	2,573	1,569
$\sigma_\varphi > 30°$	3,081	1,489	1,151	2,470	1,224	923	1,621	853	695
$\sigma_\varphi > 60°$	226	178	174	210	162	150	151	119	126

Using the criteria described above, it was found that the receiver detected 119, 107, and 98 nights (out of 140 nights) with scintillation activity on one or more satellite links for the L1, L2C, and L5 frequencies, respectively, during the period of measurements. Alone, these numbers are impressive. However, the numbers in Table 1 provide a more detailed and realistic picture of the amplitude and phase scintillation activities in the region. The differences in number of measurements for the three frequencies reflect the fact that the GPS constellation is a mix of different generations of satellites, which have been undergoing a modernization process over the years. The L2C signal is present in the IIR-M and IIF blocks, while L5 is present only in the improved IIF block. Thus, while the GPS constellation had 31 satellites transmitting the L1 signal, only 15 and 8 satellites transmitted the L2C and L5 signals, respectively, during the measurement period. Table 1 indicates that (1) $S_4 = 0.3$ was exceeded by 6.90%, 8.53%, and 9.44% of the valid samples, while $\sigma_\varphi = 10°$ was exceeded by 5.53%, 5.78%, and 5.94% of the valid samples for the L1, L2C, and L5 signals, respectively, between 19:00 LT and 02:00 LT; (2) $S_4 = 0.7$ was exceeded by 1.00%, 1.71%, and 2.70% of the valid samples, while $\sigma_\varphi = 30°$ was exceeded by 1.00%, 1.36%, and 1.76% of the valid samples for the three signals, respectively, during the same time interval. The above percentages were obtained by dividing every number in the columns (19:00 LT–01:59 LT) of Table 1 by the corresponding upper element (total). Additionally, (3) 38.81%, 35.23%, and 29.68% of the amplitude scintillation activity ($S_4 > 0.3$) was concentrated in the (20:00 LT, 21:59 LT) interval, while 66.87%, 59.33%, and 53.39% of the same activity was concentrated in the (20:00 LT, 22:59 LT) interval for the three signals, respectively. The above percentages were obtained from the division of the element of row ($S_4 > 0.3$) associated with a frequency and restricted time interval by the corresponding value for the same row, frequency, and full time interval (19:00 LT–01:59 LT), followed by multiplication of the result by 100. For example, the first percentage in (3) is obtained from $100 \times 8234/21{,}214 = 38.81\%$. Applying the same operations to the elements of row ($\sigma_\varphi > 10°$) of Table 1, one concludes that (4) 41.20%, 40.53%, and 40.28% of the phase scintillation activity was concentrated in the (20:00 LT, 21:59 LT) interval, while 71.41%, 66.48%, and 65.06% of the same activity was concentrated in the (20:00 LT, 22:59 LT) interval for the three signals, respectively.

Figure 1 shows one example of S_4 and σ_ϕ estimates at the L1, L2C, and L5 signals transmitted by PRN 25 on the night of 13 November 2014. It illustrates a case of strong amplitude and phase scintillation event, with S_4 exceeding 1.0 at the three frequencies and σ_ϕ exceeding 100° at L2C and L5 during several consecutive minutes. Figure 1a also shows the relative total electron content (TEC) for this example, where it is possible to note the strong gradients during the period of scintillation occurrence. The data gaps indicate the time intervals when, due to very intense scintillation, the receiver was unable to estimate TEC. Most of the gaps occurred when $S_4 > 1.0$. It may be noted that the TEC variation signature is the results of a large plasma bubble (that is, magnetic field-aligned plasma depletion) zonally drifting eastward. It is observed that the scintillation intensity (during its occurrence) has a minimum near 20:30 LT, which corresponds to the minimum in the TEC variation, and the two scintillation maxima correspond to the regions of TEC gradients on either sides of the minimum. This relative locations of the scintillation maxima with respect to the TEC gradient appears to be indicative of the cascading process which generates secondary (smaller-scale) plasma irregularities [*Haerendel*, 1973], operating at the steep walls of an evolving large-scale bubble structure. The scintillation intensity appears to be stronger from the TEC gradient (near 20:40 LT) at the western wall of the eastward drifting plasma depletion, which agrees with the previous observational results showing preference of irregularity development at the west wall of a developing bubble [*Tsunoda*, 1983; *Tulasi Ram et al.*, 2012].

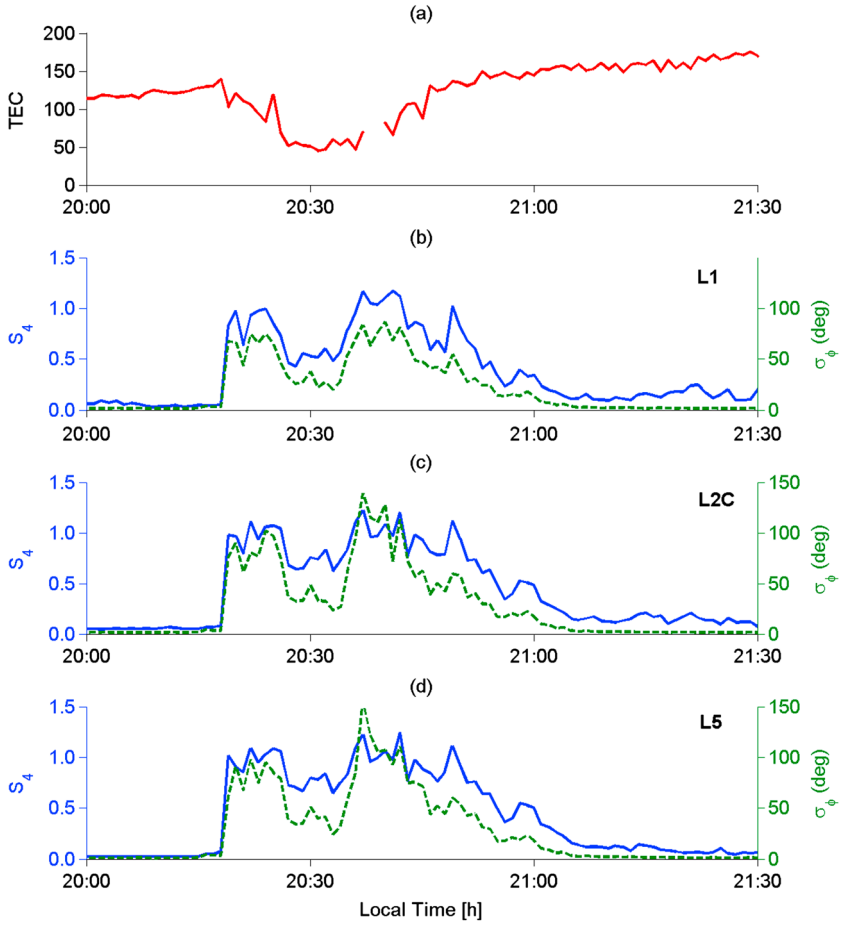

Figure 1. (a) The relative TEC for PRN 25 on 13 November 2014 in TEC units (10^{16} el/m^2). (b)–d) The corresponding S_4 and σ_φ indices for the L1, L2C, and L5 signals, using the combinations (blue continuous lines, left vertical axes) and (green dashed lines, right vertical axes), respectively.

In addition to the description of the data set provided by Table 1, Figure 2 shows the complementary cumulative distributions functions (CCDFs) of S_4 and σ_φ for the L1, L2C, and L5 signals. The distributions in Figures 2a and 2b use the data set corresponding to the interval (19:00 LT to 02:00 LT), restricted by the above selection criteria. The inflection points in Figures 2a and 2b indicate that roughly 80% of the S_4 values are less than 0.15 and 85% of the σ_φ values are less than 3.2°, independently of frequency. One would expect the severity of phase scintillation to follow the inverse of the signal frequency. The results in Figure 2 not only confirm this expectation but also empirically quantify the dependence of phase scintillation on the frequency. Therefore, it is possible to state that users of the new civil signals will be more susceptible to the effects of the ionosphere in low latitudes, distributed over a slightly wider local time interval.

Figure 2 and the percentages quoted in the previous paragraph clearly indicate that any statistical analysis of the full data set would be overwhelmed by negligible amplitude and phase scintillation. To closely study scintillation that may affect the performance of GPS receivers, lower thresholds will be specified for S_4 and σ_φ, in alignment with other authors [*Xu et al.*, 2012; *Jiao and Morton*, 2015]. To guide the selection of these thresholds, the CCDFs of the amplitude and phase data recorded during the daytime period from 10:00 LT to 14:00 LT (for all days of the campaign, but restricted by the same selection criteria) were obtained. They indicated that $S_4 = 0.2$ and $\sigma_\varphi = 3.5°$ were exceeded by less than 1% of the corresponding samples, confirming that the scintillation events were, in fact, associated with typical nighttime ESF. Based on these results and to clearly separate daytime data from spread *F* effects, the thresholds $S_4 > 0.3$ and $\sigma_\varphi > 10°$ will be adopted as indicators of noticeable amplitude and phase scintillation, respectively,

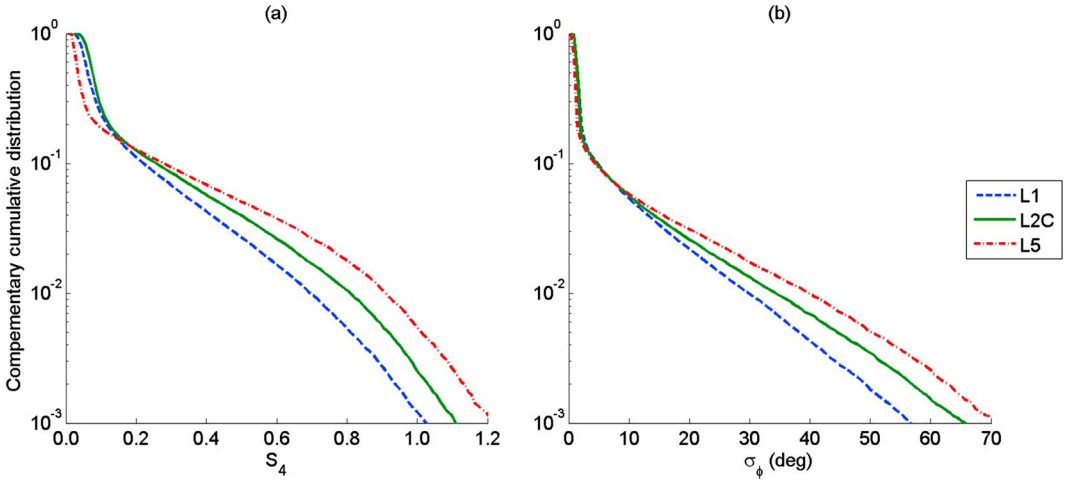

Figure 2. Complementary cumulative distributions of S_4 and σ_φ for the L1, L2C, and L5 signals. (a and b) Consider all measurement results restricted only by the selection criteria specified in the text.

when suitable to each study discussed in the next sections. Note that these thresholds are comparable to the ones selected by the above authors.

3. On the Occurrence Rate and Intensity of Scintillation

This section describes the scintillation values that GPS L1, L2C, and L5 carriers may experience under different geophysical settings, assuming $S_4 > 0.3$ and elevations $\varepsilon > 30°$. That is, the discussions in the present section will be based on 21,214; 9370; and 6187 samples for the three frequencies, respectively, according to Table 1.

Following the statistical analysis of the S_4 and σ_φ variabilities presented in the previous section, the distributions of these indices as functions of local time were investigated. The bar charts of Figure 3 show these distributions from 19:00 LT to 02:00 LT, in 30 min intervals. This 7 h period was the time interval during which all the relevant scintillation events occurred. Figures 3a, 3c, and 3e correspond to the S_4 and σ_φ indices, respectively. Figures 3b, 3d, and 3f correspond to the L1, L2C, and L5 frequencies, respectively. To obtain the number of occurrences for a given color-coded index range, its lower reading at the vertical axis should be subtracted from its upper reading. For example, the number of occurrences of $\sigma_{\varphi L1}$ in the range (15°, 30°) during the time interval (22:00 LT, 22:30 LT) observed in Figure 3b is approximately equal to 2750–1700 = 1050. To account for the large differences in the total number of samples among the three frequencies, the vertical scales of the bar charts were appropriately adjusted.

It is noted in the histograms for $S_4 < 0.6$ and $\sigma_\varphi < 30°$ associated with the L1 frequency in Figures 3a and 3b that amplitude and phase scintillation only start around 20:00 LT and reach the occurrence peaks between 22:00 LT and 22:30 LT. The peaks are relatively broad, lasting around 2 h. This behavior is similar to the one displayed by *Gwal et al*. [2006] for amplitude scintillation at Chiang Rai, Thailand (19.57°N, 99.52°E) during the quiet evenings of the equinox months. However, the scintillation occurrence peak for that site during the quiet evenings of the months around the December solstice was observed at 20:30 LT. A local time distribution of amplitude scintillation at the L1 frequency was recently reported by *Jiao and Morton* [2015] for Jicamarca, Peru (11.9°S, 76.9°W), using a 332 day data set recorded from November 2012 to July 2014. Their single distribution combines all amplitude scintillation values from all seasons, differently from the ones in Figure 3a. The Jicamarca distribution starts 1 h earlier, increases more slowly to the same peak at 22:00 LT, and decreases faster than the histogram for $S_4 < 0.6$ in Figure 3a. *Xu et al*. [2012] collected L1 amplitude and phase scintillation data in July and August 2012 at Hok Tsui, Hong Kong Island (22.20°N, 114.25°E). Their hourly histograms for $S_4 < 0.6$ and $\sigma_\varphi < 34°$ show significant amplitude and phase scintillation activity after 00:00 LT, which differ from the decreasing trends observed in the corresponding histograms displayed in Figures 3a and 3b, respectively. The earlier start time of the scintillation at the dip equatorial station Jicamarca with later onset times in our data and in the Hong Kong Island data analyzed by *Xu et al*. [2012]

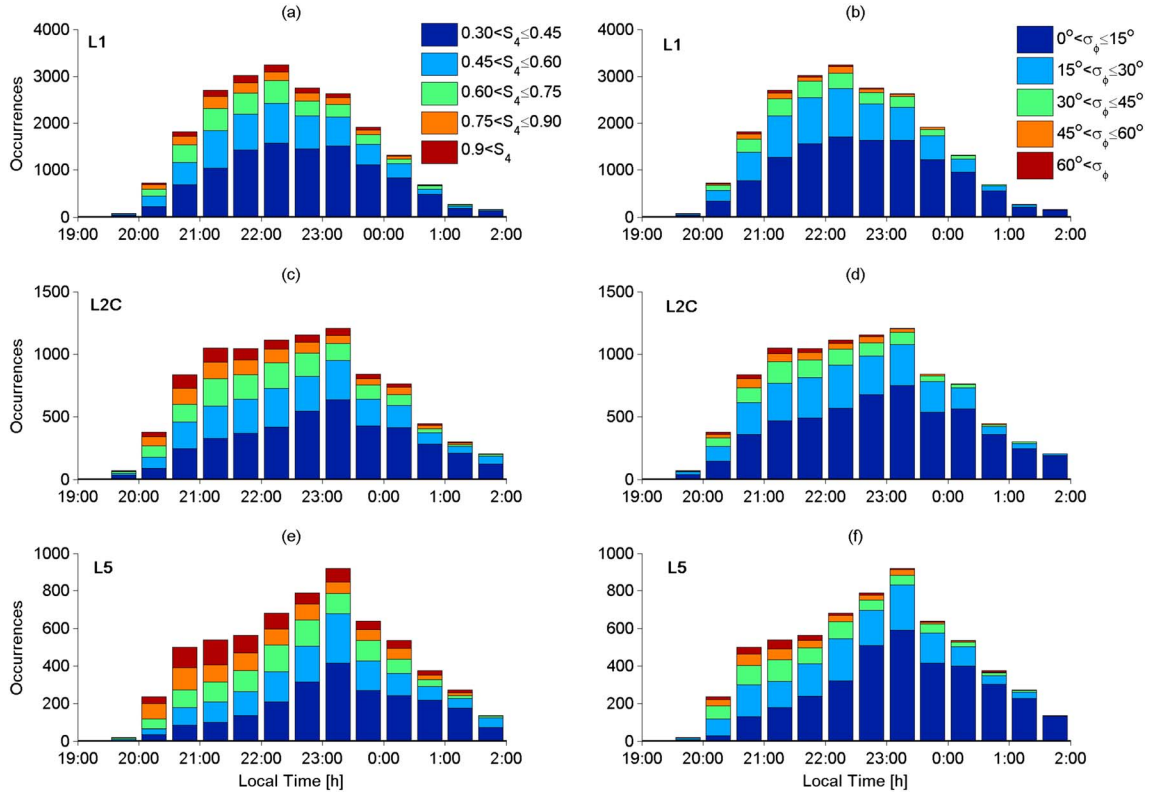

Figure 3. Histograms of the (left) S_4 and (right) σ_φ indices as functions of local time intervals, assuming $S_4 > 0.3$. The bar charts correspond to the (top) L1, (middle) L2C, and (bottom) L5 frequencies, respectively.

is consistent with the irregularity development process marked by vertical rise of flux tube-aligned bubbles over the dip equator (briefly described earlier).

The corresponding histograms (that is, for $S_4 < 0.6$ and $\sigma_\varphi < 30°$) for the L2C and L5 frequencies in Figures 3c–3f are reasonably similar to those of the L1 frequency, but the occurrence peaks are reached later, around 23:00 LT to 23:30 LT, and last only about 1 h. During the absolute peak intervals for the above scintillation levels, the $S_4 < 0.6$ cases represent 75.1%, 78.6%, and 73.7% of the total cases at the L1, L2C, and L5 frequencies, respectively. Correspondingly, the $\sigma_\varphi < 30°$ cases represent 84.7%, 89.4%, and 90.3%, respectively. Then, the scintillation occurrences gradually decrease, being extremely rare after 02:00 LT.

Figure 3 also shows that the hourly distributions of the moderate-to-strong amplitude and phase scintillation ($S_4 > 0.6$ and $\sigma_\varphi > 30°$) are somewhat different from those of their weaker counterparts. While those scintillation levels also begin around 20:00 LT, their peak occurrences are observed at least 1 h earlier than that of the weaker scintillation cases, that is between 21:00 LT and 21:30 LT for all frequencies. The moderate-to-strong scintillation occurrences remain the same for about 1 h, and then sharply decrease and become extremely rare after 01:00 LT. On the other hand, the hourly distributions of L1 moderate-to-strong amplitude and phase scintillation over Hong Kong displayed by *Xu et al.* [2012] showed significant activity after 00:00 LT, particularly for July 2012. During the peak interval for the present scintillation levels, the cases $S_4 > 0.6$ constitute 31.9%, 44.2%, and 61.4% of the total cases at the L1, L2C, and L5 frequencies, respectively. Correspondingly, the $\sigma_\varphi > 30°$ cases constitute 20.4%, 26.8%, and 41.0% of the total cases at the three frequencies. The alarming fact is that in the cases with noticeable amplitude scintillation (that is, with $S_4 > 0.3$) during the peak interval, those that display $\sigma_\varphi > 60°$ constitute 2.2%, 4.0%, and 8.7% of the total cases at the three frequencies, respectively. It is further observed that all the above percentages increase as the GPS frequencies decrease. The elevated scintillation values discussed in the present paragraph may lead receiver loops to fail during carrier tracking procedures, resulting in a loss of performance for precision positioning applications in particular.

Another aspect worth mentioning is the duration of scintillation events with $S_4 > 0.3$ for the satellites that transmit the three signals. An independent processing (from those leading to the previous results and figures) showed that scintillation at the L5 frequency lasted longer than that at the L1 and L2C frequencies in 89.44% and 66.11% of the cases, respectively. The average durations of scintillation events were 34.25, 29.95, and 27.09 min for the L5, L2C, and L1 frequencies, respectively. For the analyzed period and the satellites that transmit the three signals, there were totals of 21,214; 9370; and 6187 scintillation minutes (with $S_4 > 0.3$) at the L5, L2C, and L1 frequencies, respectively.

4. On the Spatial Distribution of σ_ϕ and S_4

As explained in section 1, the nonlinear evolution of the R-T instability causes the field-aligned EPBs rise up to the topside ionosphere, with their extremities extending to lower latitudes. The scintillation producing irregularities develop at the steep density gradient regions of the rising bubbles. Each EPB can extend several degrees in latitudes and several hundred kilometers in the east-west and vertical directions.

Knowledge of the spatial distribution of the irregularities is very important to evaluate the scintillation impact on receivers of GNSS systems in low-latitude regions. In particular, this information may be useful to users of aeronautical and augmentation systems based on GNSS. In this context, it should be noted that there are two situations leading to more intense scintillation. One is the presence of the larger background plasma density that exists in the crest region of the equatorial ionization anomaly (EIA), wherein the ΔN values are larger and therefore produce larger scintillation, as explained in section 1. The other factor is the degree to which segments of signal propagation paths become closer to being aligned with the field-aligned plasma bubble structures. A longer field-aligned propagation segment, permitting close to end-on view of the bubble irregularities, can cause more intense amplitude and phase scintillations. This arises because, obviously, the signal propagation path affected by the turbulent region associated with the plasma bubble is longer in this case than in any other orientation of the propagation path. For this reason, the geomagnetic declination and inclination angles associated with the GNSS signal ionospheric penetration point (IPP) distribution are controlling factors for the scintillation intensity distribution surrounding a receiving site. These aspects will be examined below, with the help of scintillation distribution plots as functions of azimuth, elevation, and propagation angles.

Figure 4 shows the azimuth and elevation distributions of phase scintillation observed by the São José dos Campos receiver. The top, middle, and bottom rows of plots refer to the L1 (Figures 4a–4c), L2C (Figures 4d–4f), and L5 (Figures 4g–4i) frequencies, respectively. The data set used in this figure was limited to measurements made between 21:00 LT and 23:00 LT, when the most intense scintillation events were observed. Scintillation cases with $S_4 > 0.3$ and $\varepsilon > 30°$ were used, the number of corresponding samples being 11,714; 4368; and 2573 at the three frequencies, respectively.

Figures 4a, 4d, and 4g show σ_φ values for all 350 km ionospheric penetration points (IPPs) in azimuth-elevation plots centered at the receiver, adopting the bottom-left color scale to represent the standard deviation of phase scintillation (degrees). Note that consecutive orbits show very small day-to-day variations in latitude and longitude during the 150 days of the observational campaign. Thus, the numbers of samples quoted in the previous paragraph essentially overlap in the plots along the orbits. These figures were designed to favor the visualization of intense phase scintillation cases. The different operation stages of the GPS constellation regarding the three carriers clearly affected the results displayed in these figures. Indeed, the numbers of available cases decrease together with the number of satellites transmitting each carrier.

Figures 4a, 4d, and 4g are consistent among themselves, in the sense that, broadly speaking, phase scintillation affecting L5 transmissions also affected L2C and L1 transmissions along the same raypaths. These figures indicate the predominance of moderate-to-strong phase scintillation levels ($\sigma_\varphi > 30°$) in the northern region (quadrants) and at low to moderate elevation angles (30° to roughly 60°) for the three frequencies. This result, particularly evident in Figure 4a associated with L1 transmissions, may be due to the fact that the ambient plasma density and the TEC must be stronger in the northern sector over the receiver, which must be associated with the location of the EIA crest at latitudes closely northward of São José dos Campos. It may be noted in particular that though scintillation (and therefore the bubble irregularities) extends to regions southward of the receiver site, its intensity is notably weaker than that in the

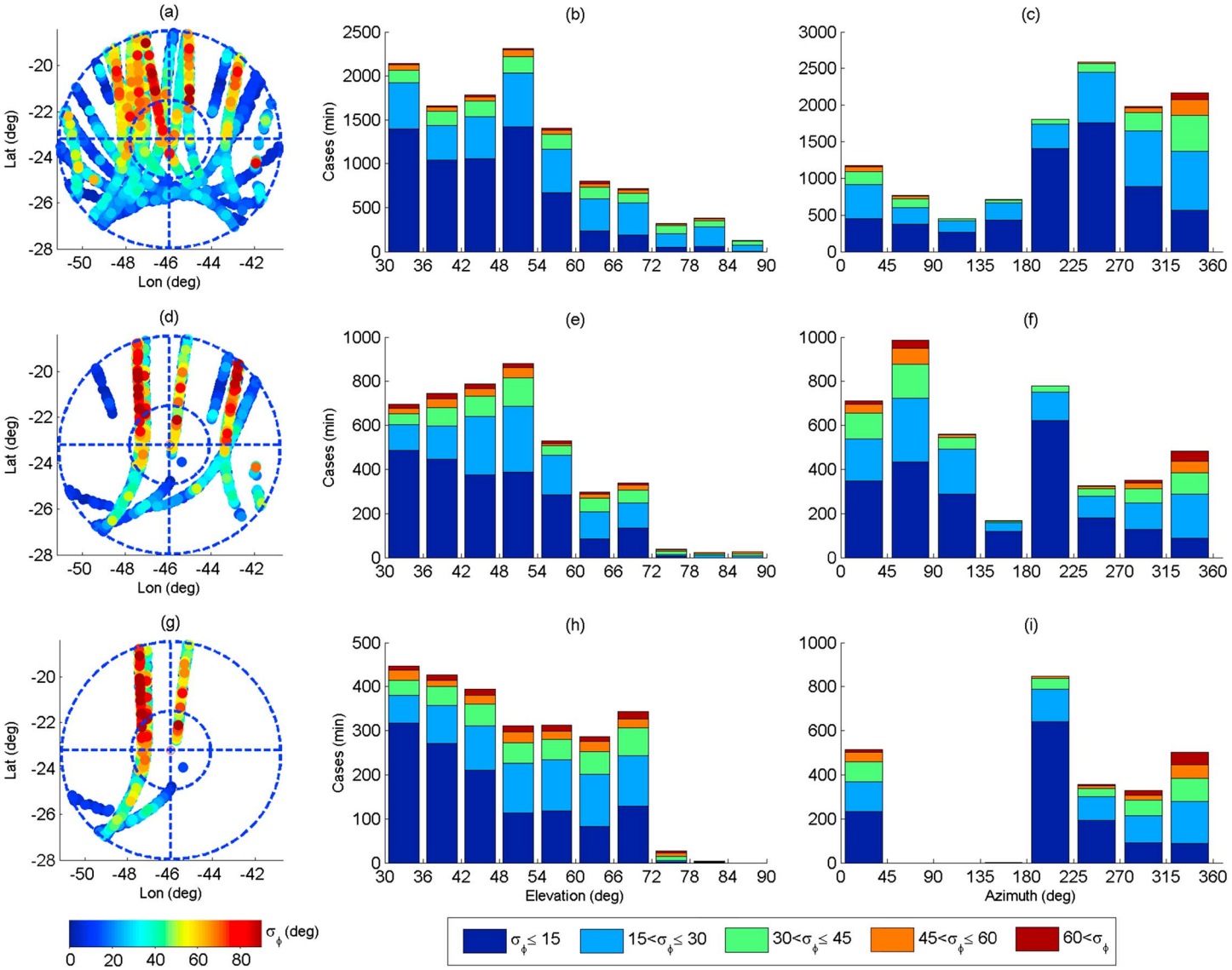

Figure 4. The spatial distribution of phase scintillation events. Results for (a–c) L1, (d–f) L2C, and (g–i) L5 measurements are presented. Figures 4a, 4d, and 4g show the azimuth-elevation spatial distribution of phase scintillation. Figures 4b, 4e, and 4h show the statistical distribution of σ_φ as a function of elevation. Figures 4c, 4f, and 4i show the statistical distribution of σ_φ as a function of azimuth.

northern sector at all the three transmissions. The absence of any scintillation in the extreme southern regions is also noticed. This observation may be attributed to the situation where the vertical growth of the bubbles was not sufficient for them to reach the magnetic field line apex heights that map to these southern regions (during the geophysical conditions that prevailed during the measurements). Another noteworthy feature is the intense scintillation events that are concentrated in the northwest quadrant, appearing to be aligned in the magnetic meridian (the declination angle over the SJC region is 21.4°W). This feature may be attributed to the propagation path being in closer alignment with the field-aligned bubble structures and therefore has important consequences for scintillation enhancement leading to the occurrence of loss of lock of the GNSS signals, which will be discussed soon. The existence of orbits with low σ_φ values interspersed with other ones displaying moderate and high σ_φ values is also observed. This is exemplified by the sequence of orbits located between the azimuths 345° and 60° in Figures 4a and 4d. Unfortunately, the absence of orbits in relatively wide azimuth sectors of the two northern quadrants prevents any additional elaboration of this observation. *Xu et al.* [2012] adopted the elevation threshold of 10° to plot the spatial distribution of L1 phase scintillation at

Hok Tsui, Hong Kong Island (22.20°N, 114.25°E), in the same format of Figure 4a. More than half of their phase scintillation data corresponded to elevations below 30°, and virtually, no moderate-to-strong phase scintillation ($\sigma_\varphi > 34°$) was observed for elevations above 45°. Most of their phase scintillation observations were associated with IPPs in the southern sector of the field of view. Considering that the above Asian site is near (and somewhat northward of) the northern crest of the equatorial anomaly (geomagnetic latitude and declination equal to 17.6°N and 2.5°W, respectively), their observations consistently support the above explanation.

Since the present IPP plots overlay data and favor intense phase scintillation, it is difficult to infer details of the σ_φ elevation and azimuth distributions from them. The bar charts representing the elevation distributions of σ_φ, using 6° elevation intervals centered at $33° + 6°n$, with $n = 0,\ldots, 9$, are provided by Figures 4b, 4e, and 4h for the L1, L2C, and L5 frequencies, respectively, using the color scale at the bottom right of Figure 4. The results show that most scintillation events occur between the elevation angles 30° and 72°. It is observed that the number of cases with lower values of phase scintillation ($\sigma_\varphi < 30°$) are relatively well distributed in the elevation interval $30° < \varepsilon < 54°$, with a discrete peak around 51° for the L1 and L2C signals. However, for the L5 signal, the same phase scintillation values are similarly distributed in the narrower interval $30° < \varepsilon < 48°$, with the same peak occurring around 33°. It is noticed that higher values of σ_φ (greater than 30°) are more evenly distributed over a wider interval ($30° < \varepsilon < 72°$) than lower ones. It is also interesting to note that the proportion of elevation angles with $\sigma_\varphi > 60°$ for the L5 signal is relatively higher than those for the other two. This is another indication of a greater susceptibility of the signal at the new frequency to ionospheric irregularities in comparison with that of the L1 signal.

Figures 4c, 4f, and 4i show bar charts representing the σ_φ azimuth distributions at 45° intervals for the L1, L2C, and L5 frequencies, respectively. These charts, which share the same color scale with the elevation plots, mainly confirm in quantitative terms the predominance of high σ_φ values between azimuths 315° and 360°. It appears evident that the high occurrence of intense scintillation in northwest azimuth sector could be associated with the westward magnetic declination of the São José dos Campos site (21.4°W). Signals received from this sector are more likely to propagate a longer distance in the turbulent medium created by the EPBs, which are aligned with magnetic field lines, becoming more vulnerable to interruptions due to loss of phase lock.

To evaluate the effect of loss of lock due to end-on view of the bubble irregularities, the angle between the propagation path and the geomagnetic field directions was calculated at the IPPs for all cases of loss of phase lock experienced by the L1 signal during the observational period. Next, this angle was projected onto (1) the magnetic meridian vertical plane and (2) the horizontal plane, at the IPPs. The first projection (β) measures the difference between the path elevation and the geomagnetic inclination. The second projection (γ) represents the difference between the path azimuth and the geomagnetic declination. The results are presented in Figure 5. Figure 5a shows that the largest number of cases of loss of lock occurred for values of β in the range 0° to 15°, while the corresponding values of γ displayed in Figure 5b were in the range of 0° to 10°. These angles correspond to the GNSS signal propagation path approaching alignment with the geomagnetic field lines. The statistics of the S_4 values plotted in Figure 5c shows that the largest number of cases of loss of phase lock occurred around $S_4 = 1$. These results show for the first time, on a quantitative basis, that GNSS signals received end-on through field-aligned plasma bubbles can suffer enhancement in scintillation intensity. Such enhancement in scintillation intensity is in addition to its enhancement in the EIA crest region arising from its dependence on the background plasma density, discussed earlier.

Table 2 indicates, for each of the three frequencies, the percentage distributions of occurrences of different ranges of σ_φ within the four quadrants, taking the receiver position as the central reference. Note that the percentages in each column add to 100%. For $\sigma_\varphi \leq 30°$, the results show a preference for phase scintillation in the northwestern and southwestern quadrants for the L1 signal. Except for the southeastern quadrant, they show a relative balance among the other ones for L2C signal. Finally, they display again a preference for the northwestern and southwestern quadrants, with a predominance by the latter, in the case of the L5 signal. For $30° < \sigma_\varphi \leq 60°$, scintillation tends to concentrate in the northwestern quadrant for the L1 and L5 signals and in the northeastern quadrant for the L2C signal. The strongest phase scintillation ($\sigma_\varphi > 60°$) is concentrated in the northwestern quadrant, in agreement also with the distribution of the amplitude scintillation index S_4 of larger intensity associated with the cases of loss of lock presented in Figures 4 and 5.

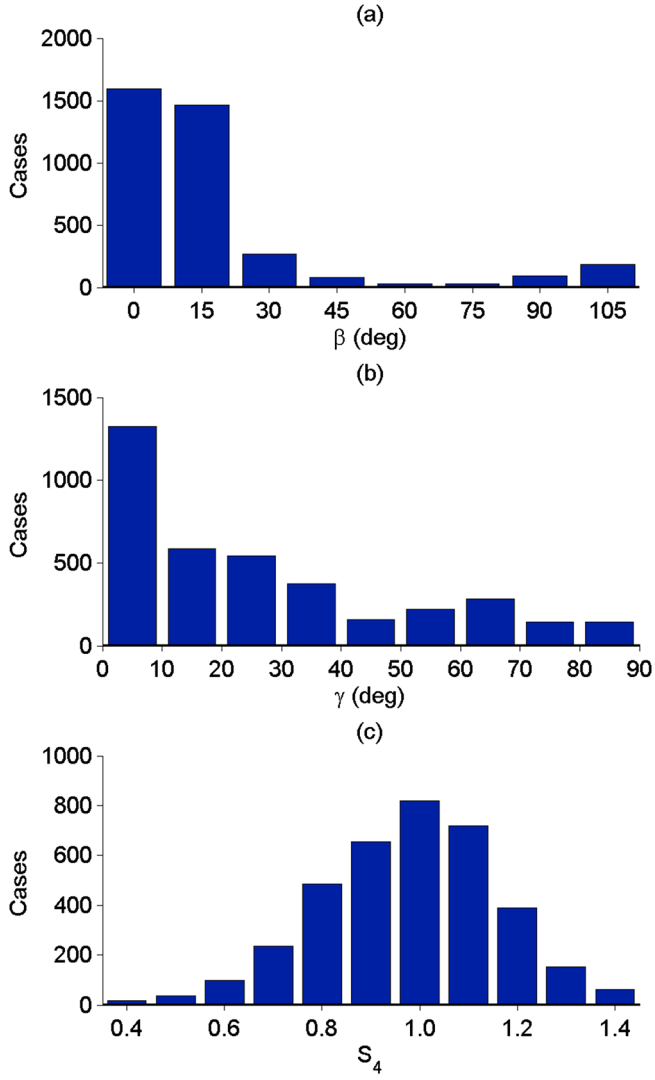

Figure 5. Angles between the GNSS signal path and geomagnetic field lines at all the IPPs that suffered loss of phase lock during the observational period, and the S_4 distribution for these cases. (a) Angular difference between the path elevation and magnetic inclination (dip angle). (b) Angular difference between path azimuth and geomagnetic declination. (c) Distribution of S_4 occurrences for cases of loss of phase lock or cycle slips.

It should again be stressed that the azimuth and elevation distributions for the three frequencies should be weighted by the different operational schedules of the GPS constellation.

5. Relationship Between S_4 and σ_ϕ for the L1, L2C, and L5 Carriers

The numbers of simultaneous occurrences of σ_φ and S_4 are shown in the maps of Figures 6a–6c for the L1, L2C, and L5 frequencies, respectively. These maps are based on 21,214; 9370; and 6187 samples for the three frequencies, respectively, that satisfy the thresholds $\varepsilon > 30°$ and $S_4 > 0.3$ and use the common scale shown in the rightmost color bar representing the number of cases. The maps consist of rectangular cells with resolutions of $\delta\sigma_\varphi = 1.67°$ and $\delta S_4 = 0.096$. It is observed that most of the occurrences are concentrated in the low-value regime of both amplitude and phase indices. The above differences in the numbers of samples and in their distributions in Figures 6a–6c are due to the operational status of the GPS constellation during the measurement period. While all the 31 satellites (16, 7, and 8 from blocks IIR, IIR-M, and IIF, respectively) transmitted the L1 signal, 15 satellites (7 and 8 from blocks IIR-M and IIF, respectively) transmitted the L2C signal and only 8 (from block IIF) transmitted the L5 signal. However, all plots indicate that there are nonnegligible numbers of simultaneous cases of high values of S_4 and low values of σ_φ, and vice versa. This feature will be further discussed below.

Figures 6d–6f show the average S_4 value as a function of σ_φ for the L1, L2C, and L5 frequencies, respectively. The average value of S_{4n} was determined for all samples of σ_φ in the interval $(5°n - 2.5°, 5°n + 2.5°)$,

Table 2. Percentage Phase Scintillation Activity for Different Sky Regions for the L1, L2C, and L5 Signals

	$\sigma_\varphi \le 30°$			$30° < \sigma_\varphi \le 60°$			$60° < \sigma_\varphi \le 90°$			$\sigma_\varphi > 90°$		
Quadrant	L1	L2C	L5	L1	L2C	L5	L1	L2C	L5	L1	L2C	L5
Northeast	17.2	31.2	16.0	29.8	48.1	36.5	19.8	42.5	23.2	20.0	36.4	8.3
Northwest	35.8	26.0	35.8	55.3	33.4	49.3	71.0	51.5	70.7	70.0	63.6	91.7
Southeast	11.5	14.3	2.7	5.6	11.0	1.2	3.2	3.0	0.6	0.00	0.00	0.00
Southwest	35.5	28.5	45.5	9.3	7.5	13.0	6.0	3.0	5.5	10.0	0.00	0.00

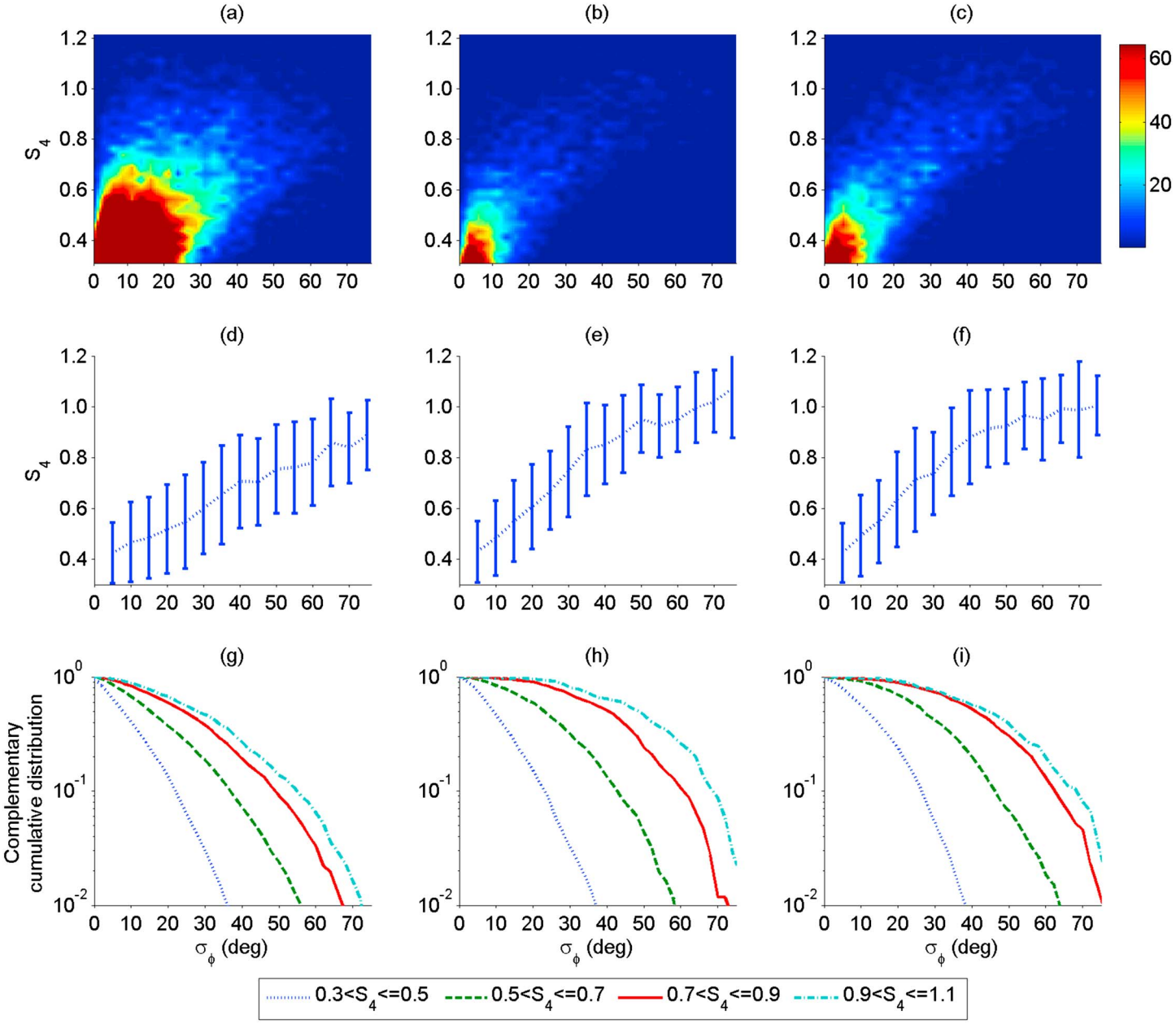

Figure 6. From left to right, the columns refer to the L1, L2C, and L5 signals, respectively. (a–c) Occurrence map for combinations of S_4 and σ_φ values, using the top-right color scale for the number of cases. (d–f) Average values for S_4 with standard-deviation bars, as functions of σ_φ. (g–i) Complementary cumulative distribution of σ_φ for different S_4 ranges.

for $n = 1, \ldots, 14$. Each of these sets of samples was also used to calculate the standard deviation of S_{4n}, represented by the error bars of the same plots. The three average functions behave similarly, displaying an increasing trend of average S_4 values with σ_φ and a change of slope near $\sigma_\varphi \approx 40°$. A closer look at these average curves indicates that those corresponding to S_{4L2C} and S_{4L5} essentially overlap. It is also observed that for $\sigma_\varphi < 40°$, S_4 increases with σ_φ at a faster rate at the lower frequencies (L2C and L5) than it does at the higher frequency (L1), whereas S_4 varies with σ_φ at the same rate at the three frequencies for $\sigma_\varphi > 40°$.

Figures 6g–6i show the complementary cumulative distribution of σ_φ for the three frequencies, considering different S_4 intervals. The L2C and L5 curves agree quite well (within 5° or less) for all probability values and selected S_4 intervals. A similar agreement holds for all curves corresponding to the lowest S_4 interval. The distributions further show (in general) that for ranges of larger S_4 values, the occurrences of larger σ_φ values also

increase. Such increases are relatively more pronounced for the L2C and L5 frequencies than those for the L1 frequency. This is another clear indication of nonnegligible numbers of simultaneous cases of high values of S_4 and low values of σ_φ, and vice versa, as also evident in Figures 6a–6c.

To further understand the nature of the relationship between σ_φ and S_4, their correlation coefficient, as defined by *Papoulis and Pillai* [2002]

$$\rho = \frac{\mathrm{cov}(S_4, \sigma_\phi)}{\mathrm{std}(S_4)std(\sigma_\phi)} = \frac{E[S_4\sigma_\phi] - E[S_4]E[\sigma_\phi]}{\sqrt{\{E[S_4^2] - E^2[S_4]\}\{E[\sigma_\phi^2] - E^2[\sigma_\phi]\}}} \quad (1)$$

was calculated. In equation (1), cov(,) is the covariance between two random variables and std is the individual standard deviation. The correlation coefficient is an important factor in the analysis of GNSS receiver performance. Indeed, *Moraes et al*. [2014] considered the correlation coefficient in their estimations of the receiver tracking loop errors. Depending on the value reached by ρ, the tracking errors may increase by up to 25%. That is one of the motivations for the statistical characterization of ρ. This calculation was applied to the set of synchronized and cofrequency σ_φ and S_4 values resulting from all sections of satellite orbits with: (1) 10 minute duration, (2) all elevations above 30°, and (3) all samples with $S_4 > 0.3$.

Figures 6d–6f have already indicated well-defined relations between σ_φ and the average value of S_4. Now Figures 7a–7c present the distributions resulting from the correlation coefficient calculations between S_4 and σ_φ at the L1, L2C, and L5 frequencies. These plots confirm most records of cofrequency σ_φ and S_4 and are highly correlated. However, the correlation can also be low for a substantial number of cases. The average correlation coefficient is approximately equal to 0.65. Figures 7d–7i illustrate six examples of relationships between σ_φ and S_4 for decreasing values of ρ. Note that the vertical scales for σ_φ and S_4 were adjusted in each panel for the corresponding curves to superpose to the possible extent. Figure 7d shows a highly correlated example ($\rho = 0.91$). Except for the two peaks with high values of σ_φ and S_4 near 1 (indicating saturation), the superposition between the curves is almost perfect. This assessment extends to most sections of the curves displayed in Figure 7e, where $\rho = 0.81$. A difference between them is observed between 22:40 LT and 23:10 LT, as well as in a few localized peaks and notches. Figure 7f shows an example with $\rho = 0.62$, which is close to the average value, with σ_φ and S_4 time series displaying different decreasing trends after 21:15 LT. Figures 7g–7i show different examples with moderate to low values of ρ, exhibiting increasing disagreement between phase and amplitude indices. The large-scale behaviors of the σ_φ and S_4 curves in Figure 7g are similar. However, long periods of relatively smooth variations of one index accompanied by fast oscillations of the other are also observed. In Figure 7i, S_4 displays a relatively fast initial increase to a moderate level, which is not followed by σ_φ. The differences in the fluctuation patterns of σ_φ and S_4 between 23:10 LT and 23:25 LT also contribute to a decreased value of the correlation coefficient.

Another aspect worth discussing is the occurrence of intense amplitude scintillation and weak phase scintillation, and vice versa. Table 3 displays the number of single or simultaneous observations of S_4 and σ_φ using different thresholds, for the three carriers, assuming satellite elevations greater than 30°. Note that Table 3 is divided into three vertical blocks. Each vertical block is additionally divided into upper and lower subblocks. For convenience, some of the numbers previously presented in Table 1 have been repeated in Table 3. The top-left subblock considers noticeable amplitude scintillation ($S_4 > 0.3$) and weak phase scintillation ($\sigma_\varphi \leq 10°$), which corresponds to 39.14%, 41.60%, and 40.75% of the cases of noticeable amplitude scintillation and unrestricted phase scintillation for the L1, L2, and L5 frequencies, respectively. They are relatively high and remain approximately independent of the GPS frequencies. The bottom-left subblock considers weak amplitude scintillation ($S_4 \leq 0.3$) and noticeable phase scintillation ($\sigma_\varphi > 10°$), which corresponds to 24.13%, 13.80%, and 5.88% of the cases of unrestricted amplitude scintillation and noticeable phase scintillation for the three frequencies, respectively. These percentages clearly decrease faster than the GPS frequencies. On the other hand, the top-right subblock considers strong amplitude scintillation ($S_4 > 0.7$) and weak phase scintillation ($\sigma_\varphi \leq 10°$), which corresponds to 11.48%, 7.82%, and 6.40% of the cases of strong amplitude scintillation and unrestricted phase scintillation for the three frequencies, respectively. These relatively small but nonnegligible percentages also decrease faster than the GPS frequencies. Finally, the bottom-right subblock considers weak amplitude scintillation ($S_4 \leq 0.3$) and strong phase scintillation ($\sigma_\varphi > 30°$), which corresponds to 1.27%,

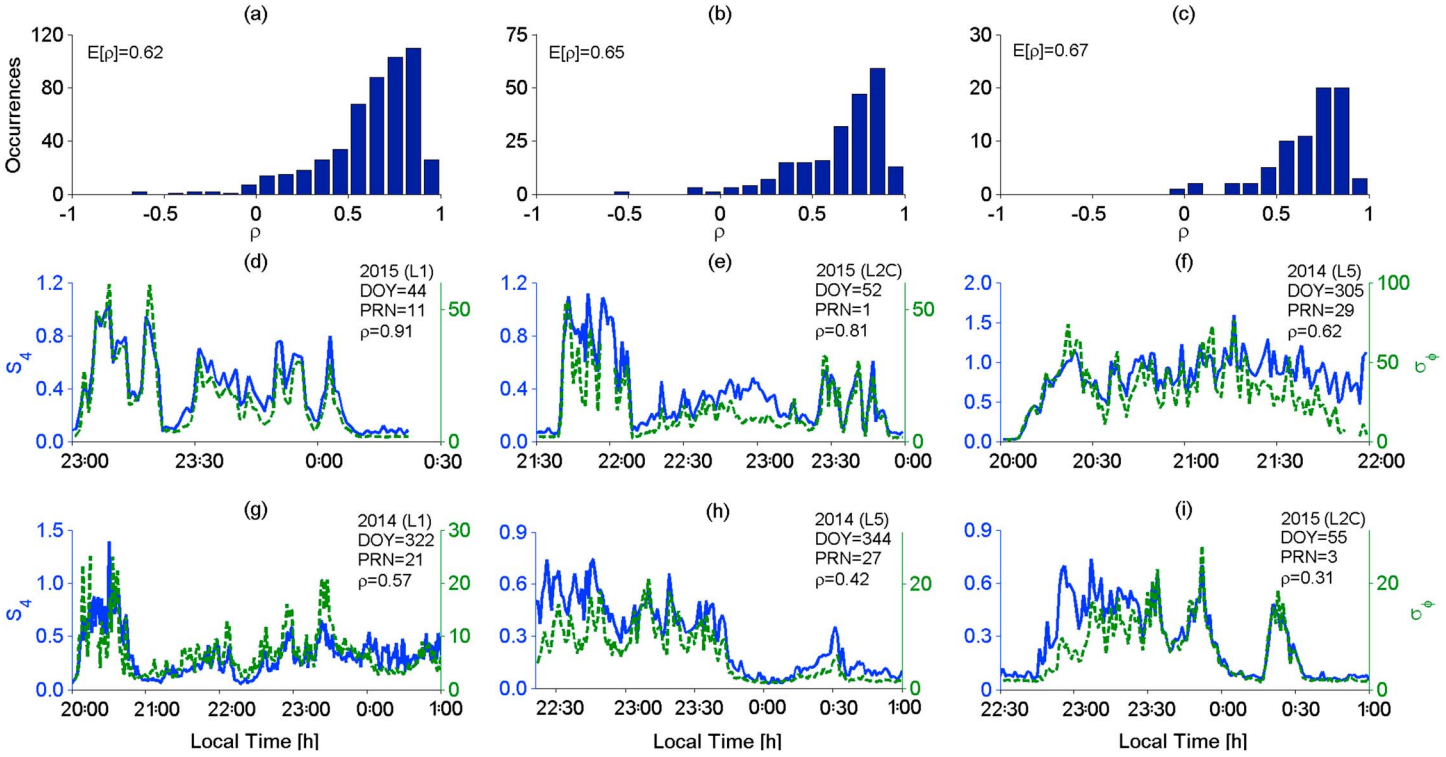

Figure 7. (a–c) The distribution of the correlation coefficient ρ for the L1, L2C, and L5 signals, respectively. (d–i) Several examples of the S_4 and σ_φ relation for decreasing values of ρ.

0.20% and 0.09% of the cases of unrestricted amplitude scintillation and strong phase scintillation for the three frequencies, respectively. These results seem to indicate that the combination of intense amplitude scintillation and weak phase scintillation is more common than the opposite.

To complement the information of Table 3, Figures 8a, 8c, and 8e show the conditional bar charts for S_4 (>0.3, indicating noticeable to strong amplitude scintillation) assuming $\sigma_\varphi \leq 10°$ (indicating weak phase scintillation) for the three GPS frequencies. Note that the bars in each of these S_4 plots (from top to bottom) add up to 39.13%, 41.60%, and 40.75%, respectively, as explained in the previous paragraph. These plots indicate that the conditional percentages decrease exponentially, according to the model $p_{S_4} = ae^{-bS_4}$. Additionally, Figures 8b, 8d, and 8f show the corresponding bar charts for σ_φ (>10°, indicating noticeable to strong phase scintillation) assuming $S_4 \leq 0.3$ (indicating weak amplitude scintillation), together with corresponding exponential trend lines. The bars in each of these σ_φ plots add to 24.13%, 13.80%, and 5.88%, respectively. To indicate how closely the values calculated by the trend line are to the measured data, the coefficient of determination R^2, which is a number from 0 to 1, has been estimated for all bar charts of Figure 8. A trend line is most reliable when its R^2 value is equal to or near 1. In all cases, R^2 exceeded 0.99. Figure 8 shows that there are cases of noticeable or even strong

Table 3. Total Activity for Amplitude and Phase Scintillation Events for L1, L2C, and L5

	L1	L2C	L5		L1	L2C	L5		L1	L2C	L5
$S_4 > 0.3$	21,214	9,370	6,187	$S_4 > 0.5$	8,391	4,396	3,361	$S_4 > 0.7$	3,076	1,879	1,767
$S_4 > 0.3$ and $\sigma_\varphi \leq 10°$	8,302 (39.14%)	3,898 (41.60%)	2,521 (40.75%)	$S_4 > 0.5$ and $\sigma_\varphi \leq 10°$	1,728 (20.59%)	910 (20.70%)	592 (17.61%)	$S_4 > 0.7$ and $\sigma_\varphi \leq 10°$	353 (11.47%)	147 (7.82%)	113 (6.39%)
$\sigma_\varphi > 10°$	17,018	6,348	3,895	$\sigma_\varphi > 20°$	6,883	2,895	2,076	$\sigma_\varphi > 30°$	3,081	1,489	1,151
$S_4 \leq 0.3$ and $\sigma_\varphi > 10°$	4,106 (24.12%)	876 (13.80%)	229 (5.88%)	$S_4 \leq 0.3$ and $\sigma_\varphi > 20°$	418 (6.07%)	27 (0.93%)	9 (0.43%)	$S_4 \leq 0.3$ and $\sigma_\varphi > 30°$	39 (1.26%)	3 (0.20%)	1 (0.01%)

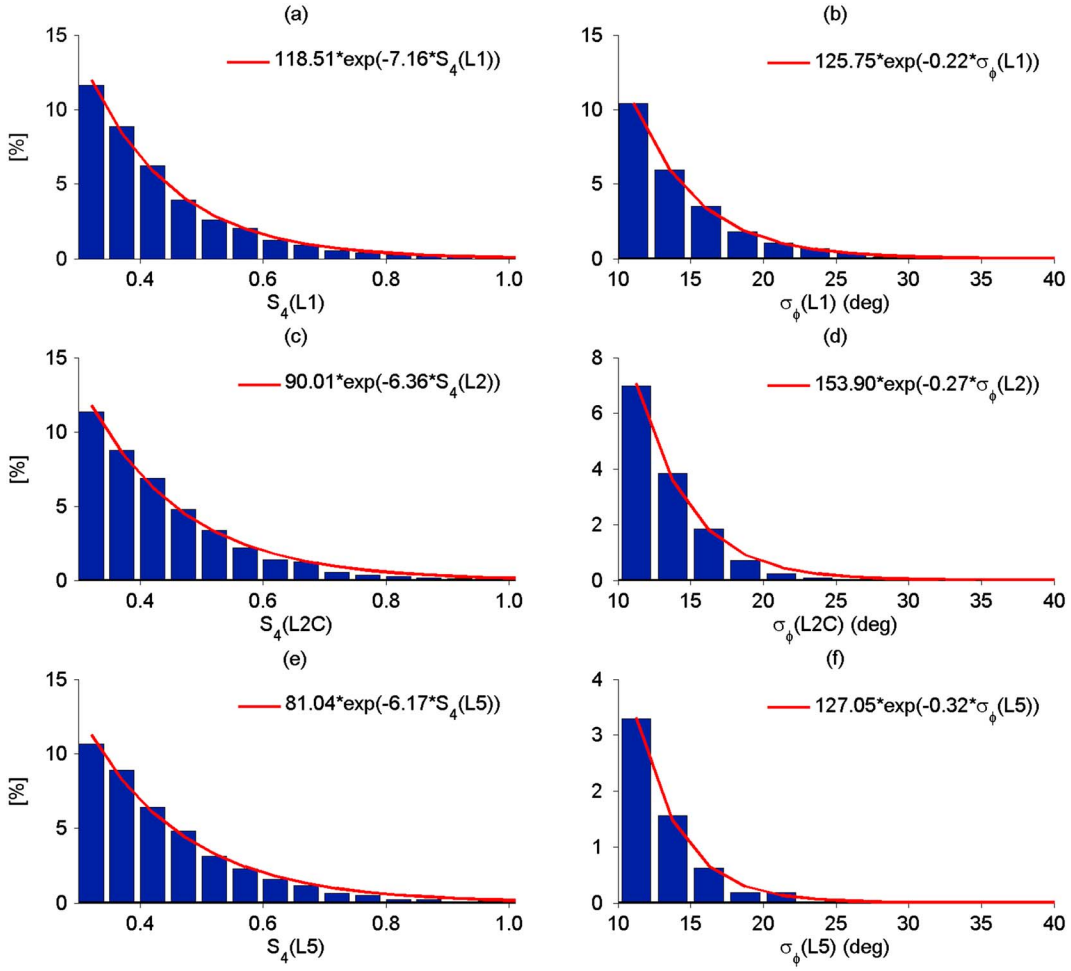

Figure 8. (a, c, and e) The conditional bar charts for S_4 (>0.3), assuming $\sigma_\varphi \leq 10°$. (b, d, and f) The conditional bar charts for σ_φ (>10°) assuming $S_4 \leq 0.3$. The top, middle, and bottom rows refer to the L1, L2C, and L5 signals, respectively. An exponential trend line has been adjusted to each bar chart. For all bar charts, the coefficient of determination R^2 is greater than 0.99 (see text for additional explanation).

amplitude scintillation accompanied by weak phase scintillation, and vice versa. However, S_4 is less than 0.5 for most of cases with $\sigma_\varphi \leq 10°$ and σ_φ is less than 17.5° for most of the cases with $S_4 \leq 0.3$. Therefore, *isolated* scintillation cases are a fact in the SJC data set, but their values do not normally reach disrupting levels. These *isolated* occurrences are more common in amplitude than in phase.

In summary, this section quantified and discussed in more detail the conclusion by *Doherty et al*. [2003] that amplitude scintillation could occur without phase scintillation, while phase scintillation was always accompanied by at least a moderate level of amplitude scintillation. This conclusion was later endorsed by *Gwal et al*. [2006].

6. Frequency Dependence of S_4 and σ_ϕ in the L Band

In this section, the GPS frequency dependence of amplitude and phase scintillation will be addressed. The goal is to verify the ratios between the scintillation indices at the lower frequencies L2C and L5 with respect to corresponding values at the widely used and higher L1 frequency for the cases of σ_φ and S_4. From the knowledge of such ratios, it would be possible to estimate the severity of the L2C and L5 scintillation based on studies using only L1 data. This analysis is particularly important for users of precision dual-frequency receivers. Another aspect to consider is the fact that the new L5 signal is intended for aeronautical applications. Knowledge of ionospheric effects at this frequency is of great use for planning

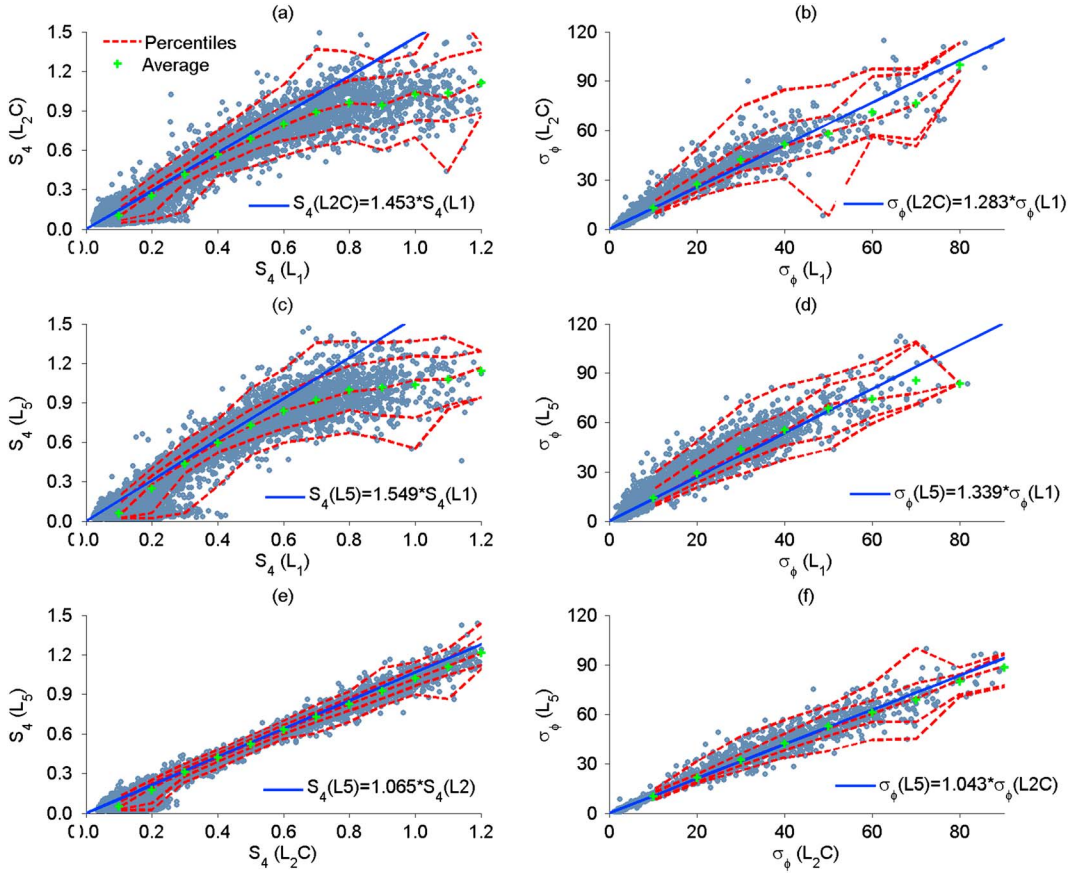

Figure 9. Scatterplots of the indices (left column) σ_φ and (right column) S_4 for all combinations of the three GPS frequencies. The blue straight lines through the origin result from equations (2) and (3), respectively (the corresponding coefficients are shown). The green crosses indicate the average of all ordinate values associated with narrow and consecutive abscissa intervals. The dashed red curves indicate 1%, 10%, 50%, 90%, and 99% percentiles, obtained by similar procedures to that utilized in the determination of the average curve.

of the corresponding systems while the GPS constellation develops to full operationality. According to *Fremouw et al.* [1978] and *Yeh and Liu* [1982], the dependence of the σ_φ and S_4 indices on the different GPS frequencies can be represented by

$$\sigma_\phi(La) = \left(\frac{f_{Lb}}{f_{La}}\right)\sigma_\phi(Lb) \tag{2}$$

and

$$S_4(La) = \left(\frac{f_{Lb}}{f_{La}}\right)^{1.5} S_4(Lb) \tag{3}$$

where *La* and *Lb* represent the combinations of the L1, L2C, and L5 frequencies with $f_{Lb} > f_{La}$. The available empirical data sets for this study are defined by pairs of simultaneous measurements ($\sigma_{\varphi Lb}$, $\sigma_{\varphi La}$) and (S_{4Lb}, S_{4La}).

Figure 9 shows scatterplots of the indices σ_φ and S_4 for all combinations of the three GPS frequencies. Figure 9 (right column), associated with $\sigma_{\varphi Lb}$ and $\sigma_{\varphi La}$, also displays blue straight lines through the origin representing their relationships according to equation (2). The coefficients resulting from the frequency ratios obtained from equation (2) are $f_{L1}/f_{L2C} = 1.283$, $f_{L1}/f_{L5} = 1.339$, and $f_{L2C}/f_{L5} = 1.044$). Also note that the green crosses indicate $<\sigma_{\varphi La}>$ values at 10° intervals along the abscissa, where $<\sigma_{\varphi La}>$ is the average of all ordinate values associated with abscissa values in the range ($10°n - 5°$, $10°n + 5°$). The blue straight lines are aligned with the corresponding average curves defined by the green crosses for $\sigma_{\varphi L1} < 70°$. Therefore, equation (2) provides

an excellent representation for the average relationship between σ_φ and the GPS frequency. The present results are also in good agreement with the results reported by *Jiao and Morton* [2015] for Jicamarca, Peru (11.9°S, 76.9°W).

Figure 9 (right column) additionally displays dashed red curves, indicating 1%, 10%, 50%, 90%, and 99% percentiles, obtained by similar procedures to that utilized in the determination of the average curve. Based on these curves, it is possible to estimate the distribution of the ordinate $\sigma_{\varphi La}$ for each range ($10°n - 5°$, $10°n + 5°$) of the corresponding abscissa. It should be noted that the percentile curves of the plots ($\sigma_{\varphi L1}$, $\sigma_{\varphi L2C}$) and ($\sigma_{\varphi L1}$, $\sigma_{\varphi L5}$) exhibit a gradual data spreading around the average line as $\sigma_{\varphi L1}$ increases. Figure 9e shows that the dispersion of the values around the average curve is less for the $\sigma_{\varphi L2C}$ versus $\sigma_{\varphi L5}$ plot than the other cases indicated immediately above, since the corresponding frequencies are very close.

Figure 9 (left column) represent the relationships between different combinations of pairs of S_{4Lb} and S_{4La} values in the same format as that in Figure 9 (right column). These plots also display blue straight lines through the origin representing equation (3) and the corresponding coefficients, which are equal to the frequency ratio raised to the power 3/2. The plots in Figures 9a and 9c indicate that this equation only represents the average relationship between the pairs (S_{4L1}, S_{4L2C}) and (S_{4L1}, S_{4L5}) in the restricted range $S_{4L1} < 0.6$. In other words, the average values of both S_{4L2C} and S_{4L5} (represented by green crosses) tend to saturate around unity well before S_{4L1} attains unity and increases beyond. On the other hand, equation (3) is an excellent representation for the average relationship between S_{4L2C} and S_{4L5} due to the proximity of these two frequencies. With the exception of the range $S_{4L1} > 0.6$, which was not considered by *Jiao and Morton* [2015], the above results are in good agreement with the ones reported for Jicamarca, Peru (11.9°S, 76.9°W). A discussion based on the percentile curves of the plots (S_{4L1}, S_{4L2C}), (S_{4L1}, S_{4L5}), and (S_{4L2C}, S_{4L5}) would also be entirely similar to the one in the previous paragraph and will be omitted.

7. Summary and Conclusions

This study presented and discussed the results of an analysis of scintillation data at the L1, L2C, and L5 frequencies recorded during 5 months (from November 2014 to March 2015) at São José dos Campos, Brazil, located near the southern crest of the equatorial ionization anomaly. Analysis has been performed on both amplitude and phase scintillation, with the corresponding characteristics of both types of scintillation relating to some key irregularity features have been examined and compared. Important aspects of local time and spatial distributions of scintillation were discussed. The unique nature of the associated plasma bubble irregularity distribution with respect to the geomagnetic field configuration that produced propagation angle dependent scintillation enhancement over the Brazilian region was also discussed. A brief summary of the main results and some conclusions are presented below.

During the period of this study, noticeable scintillation ($S_4 > 0.3$ or $\sigma_\varphi > 10°$) was present during 8% to 10% of the time interval (1900 LT to 0200 LT), while strong scintillation ($S_4 > 0.7$ or $\sigma_\varphi > 30°$) was present only during 2% to 4% of the same time interval. During the local time period of its larger occurrence probability (2000 LT to 2300 LT), the percentage concentration of phase scintillation activity (80%) was higher than that of amplitude scintillation activity (60%).

A case of TEC depletion event, marking an EPB passage across a **raypath**, was examined together with the associated variations in S_4 and σ_φ (Figure 1). It showed that scintillation occurred at the strong gradient region of the depletion and it appeared more intense at the western wall of the plasma bubble in its (expected to be) eastward drift motion. This picture supported the results from previous studies [*Tsunoda*, 1983; *Tulasi Ram et al*., 2012] that also addressed the question of colocation of smaller-scale irregularity growth associated with a developing plasma bubble.

The local time distributions of amplitude and phase scintillations (Figure 3) were examined and found to be very similar at corresponding intensity levels. In the case of phase scintillation for different intensity ranges, it was found that more than 75% of the cases corresponded to $\sigma_\varphi < 30°$. Additionally, during the absolute peak intervals for moderate phase scintillation, 76.4%, 86.8%, and 86.5% of the cases corresponded to $\sigma_\varphi < 30°$ at the L1, L2C, and L5 frequencies, respectively. These cases of scintillation ($\sigma_\varphi < 30°$) started around 1930 LT to reach its peak occurrence from 2200 LT to 2330 LT at the L1 frequency. However, the peak occurrence shifted to later hours (from 2300 LT to 2330LT) at the lower frequencies L2C and L5. The cases of stronger phase

scintillation ($\sigma_\varphi > 30°$) started around 2000 LT, the occurrence maximizing between 2100 LT and 2130 LT, 1 h earlier than the peak in weak scintillation. During the peak occurrence, the percentage of the strong cases was 34.8% at L1 and this percentage increased with the decrease in frequency, being 38.2% at L2C and 55.8% at L5.

A noteworthy observation is that the cases of $\sigma_\varphi > 60°$ that can lead to receiver loop failure during carrier tracking procedures occurred frequently between 2100 LT and 2130 LT. The total number of such occurrences during the analysis period was 462, 214, and 210 times at the respective frequencies, which is a significant problem for the safety of GNSS applications.

The local time variation of the amplitude scintillation is very similar to that of the phase scintillation, as can be easily verified by noting (in Figure 3) the similarities of the variations in different intensity ranges, such as $S_4 < 0.6$ with $\sigma_\varphi < 30°$ and $S_4 > 0.6$ with $\sigma_\varphi > 30°$.

The spatial distribution of phase scintillation, as seen from the receiver location, was examined for different ranges of σ_φ values at the three frequencies by associating each case with the azimuth and elevation angles of the respective IPP. It was noted that there is a dominance of σ_φ in the northern quadrants of the field of view. These quadrants cover the equatorial anomaly crest region of large ambient plasma density, causing enhanced scintillation. Enhanced scintillation was also present around the azimuth angle of 345° at all levels of phase scintillation. In view of the large westward magnetic declination (21.4°W) of this region, this result strongly suggested the possibility that the GPS satellite signal reception was close to being end-on through magnetic field-aligned plasma bubbles. Under this alignment, the larger propagation path length through the bubbles can result in larger scintillation intensity, as indeed observed in these cases. Further analysis based on calculation of the propagation angles with respect to the magnetic field line (in elevation and azimuth) clearly showed that cases of loss of phase lock occurred more frequently for small values of these angles, and they were distributed around values of $S_4 = 1$. Cases of scintillation enhancement over a low-latitude site in the northern hemisphere (Calcutta, India, 22.5°N, 88.3°E) as observed on GPS signals received from southern region over that station, not directly related to the enhanced EIA electron density, were attributed to nearly field-aligned satellite-to-receiver propagation paths by *DasGupta et al.* [2004]. Based on an extensive set of data samples (311,369 scintillation values), the present work has provided for the first time a quantitative verification and confirmation of the effect of scintillation enhancement due to closer magnetic field-aligned satellite-to-receiver propagation paths.

The more frequent cases of σ_φ observed in Figure 4 at elevation angles greater than 36° may be indicative of the vertical growth rate for the bubble to reach appropriate apex heights over the equator that can contribute toward EPB-aligned line of sights from the receiver. It was also noted that intense phase scintillation was observable at higher-elevation angle (around 60°) at the lower frequency (L5), though with a limited number of data samples. A most noteworthy aspect is that no significant scintillation cases could be observed from the southern quadrants (180°–270°) of the receiver field of view, which is an indication that during the observational period (November 2014 to March 2015), which is close to the recent solar maximum, the EPBs did not rise up to more than about 900 km over the equator, the apex height of the magnetic field lines that map to the *F* region over São José dos Campos.

A comparison between S_4 and σ_φ (Figure 6) for each of the three frequencies showed a well-defined relationship between them. However, there are nonnegligible numbers of simultaneous cases of high values of S_4 and low values of σ_φ, and vice versa. A somewhat linear relationship between S_4 and σ_φ values averaged over discrete intervals was observed for $\sigma_\varphi < 70°$. The corresponding average S_4 values are found to be slightly larger at the lower frequencies. Also, S_4 values tended to saturate for larger σ_φ values, exceeding around 80°. This suggests that for severe events, phase measurement can provide a better evaluation of scintillation variability than it is possible from amplitude measurement. This observation seems to also indicate that the combination of intense amplitude scintillation and weak phase scintillation is more common than the opposite case.

A detailed study showed that although most cases of σ_φ and S_4 are highly correlated, there is a substantial number of examples of poor to moderate correlations. The total percentages of weak, moderate, and strong correlation cases for the L1 frequency are 14%, 28%, and 58%, respectively. It was also found that in the lower ranges of values of σ_φ (<30°) and S_4 (<0.7), the percentages of cases with weak, moderate, and strong correlations are nearly the same (35.16%, 30.07% and 34.07%, respectively). On the other hand, for higher

values of σ_φ (>30°) and S_4 (>0.7), the corresponding percentages of the cases are 0.00%, 15.85%, and 84.15% respectively, indicating the dominance of cases of strong correlation for more intense scintillation. However, the circumstances that control the degree of correlation are not clearly identified.

A study (Figure 2) of complementary cumulative distribution functions of σ_φ and S_4 for the three frequencies provided an empirical quantification of the frequency dependence of phase and amplitude scintillation, showing that lower frequencies (L2C and L5) suffer more intense scintillation than L1. A more direct analysis on the frequency dependence of σ_φ and S_4 was carried out (Figure 9) with the objective of verifying the validity of the theoretical representations of the ratios of the scintillation indices at the different frequencies. This investigation was also carried out to support evaluations of the severity of scintillation at the new lower frequency L5 (intended for aeronautical applications) based on the values at the more widely used L1 frequency. The result showed that the ratios of phase scintillation indices were in excellent agreement with their expected values (that is, the corresponding frequency ratios) until a transition value $\sigma_\varphi \approx 70°$ at the L1 frequency is reached. In the case of amplitude scintillation (for which the expected ratio was the frequency ratio raised to the power 3/2) the transition occurred at $S_{4L1} \approx 0.6$. Above these transition values, the ratios decrease, tending to saturate with further increase in the scintillation intensity at L1. However, the scintillation ratio between the two closer frequencies L2C and L5 maintained its expected value at all levels of scintillation intensity.

As summarized above, this study has examined some of the most outstanding characteristics of amplitude and phase scintillation on GNSS signals in the region of the equatorial ionization anomaly over Brazil, where the plasma bubble activity is known to be often more intense and frequent than at other longitude sectors. This may well be one of the first such studies undertaken for a low-latitude location. A few of the main conclusions may be briefly summarized as follows: (1) a case study shows that the scintillation irregularities may form at the western wall of a developing bubble, confirming previous results; (2) local time variations show that amplitude and phase scintillation in all ranges of intensities initiate at the same local time (approximately 20:00 LT), but the stronger events attain peak intensity by 21:30 LT, earlier (by 1 to 2 h) than the weaker events, with all events decaying by about 02:00 LT; (3) scintillation intensity becomes enhanced and loss of phase lock becomes more frequent when signal propagation path segments are closer to being aligned with magnetic field lines, in addition to its enhancement due to higher background density of the EIA; (4) during the present observational period of the recent solar maximum the plasma bubble vertical extension over the equator did not exceed approximately 900 km, as indicated by the absence of scintillation southward of the present observing site; (5) phase and amplitude scintillation are well correlated in general, but at smaller scintillation intensities the cases of weak, moderate, and strong correlation between them are about the same, whereas at larger intensities the cases of strong correlation dominate; and (6) the frequency dependence of the scintillation is observed to obey its theoretical representation based on inverse frequency ratio in the case of σ_φ and that raised to 1.5 in the case of S_4 but fails to obey it beyond a transition value of scintillation at the higher frequency.

Finally, it should be pointed out that this study has clarified a number of relevant issues. However, it has also raised some important questions that need to be addressed in future investigations: detailed understanding of the relationship between σ_φ and S_4 at different phases of a bubble development, including their characteristics at the western and eastern walls of a zonally drifting EPB; departure from simple theoretical representation of the frequency dependence of scintillation at more intense events (above the transition values of σ_φ and S_4 revealed from this study); detailed understanding of the scintillation enhancement effect due to end-on view of satellites through magnetic field-aligned plasma bubbles; the circumstances that control the degree of the correlation between amplitude and phase scintillation; the role of refractive effect in phase scintillation; etc.

Several limitations of the S_4 and σ_φ indices have been discussed in the literature [*Forte and Radicella*, 2002; *Beach*, 2006; *Moraes et al*., 2014]. *Carrano et al*. [2012] proposed the iterative parameter estimate (IPE) technique to infer the parameters of an equivalent ionospheric screen from scintillation data. It assumes that all levels of low- and high-latitude scintillation (for all time sectors, seasons, levels of Sun activity, etc.) can be characterized from a two-component inverse power law irregularity spectrum which depends on six parameters: drift, Fresnel radius, turbulence strength, two power law indices, and a break scale size. This technique, which is not based on the S_4 and σ_φ, could be applied to understand the differences between high-latitude and

low-latitude scintillation. However, it is complex and time-consuming. A faster technique which could be in implemented by future-generation ISMs to provide improved real-time characterization of ionospheric irregularities under both weak and strong scintillation conditions has been recently proposed [*Carrano et al*., 2015] and could be further explored. In the meantime, S_4 and σ_φ still are the most widely used parameters in the description of ionospheric scintillation, also routinely provided by the current generation of high-quality ISMs. It should be particularly observed that the ISM used for the present study and the applied preprocessing of the raw data meet the recommendations by respected developers [*Van Dierendonck et al*., 1993; *Van Dierendonck*, 2008] and follow the conventional practice [*Doherty et al*., 2003; *Jiao and Morton*, 2015].

Another important subject for future studies is how well GPS processors perform as a function of C/N_o and fully and carefully defined scintillation inputs, considering the combined operation of PRN correlators and PLLs. These and related topics will be the focus of future investigations.

Acknowledgments

A.O.M. is grateful to CNPQ through Grant 465648/2014-2 and wishes to thank the Instituto de Aeronáutica e Espaço (IAE), where he works as a research engineer, for supporting and assisting his cooperation research with INPE and ITA. M.A. Abdu acknowledges the support received from the Coordenação de Aperfeiçoamento de Pessoal de Nível Superior (Capes) for a senior visiting professorship at ITA/DCTA. F.S.R. would like to thank the support from NSF (AGS-1554926). E.R. de Paula acknowledges the support of Conselho Nacional de Desenvolvimento Científico e Tecnológico (CNPq), through grant 310802/2015-6. The monitoring station used in this work was deployed in the context of Projects CIGALA/CALIBRA, both funded by the European Commission (EC) in the framework of the FP7-GALILEO-2009-GSA and FP7–GALILEO–2011–GSA–1a, respectively, and FAPESP Project 06/04008-2. The authors thank Jean-Marie Sleewaegen (Septentrio) for the valuable discussions and the reviewers for the insightful and constructive comments, which helped them in the development of a better paper. To request the raw data that have been used in this article, please contact Jonathan Verdeli (jonathan.verdeli@inpe.br).

References

Aarons, J. (1982), Global morphology of ionospheric scintillation, *Proc. IEEE*, *70*(4), 360–378, doi:10.1109/PROC.1982.12314.

Abdu, M. A., J. A. Bittencourt, and I. S. Batista (1981), Magnetic declination control of the equatorial F region dynamo electric field development and spread F, *J. Geophys. Res.*, *86*(A13), 11,443–11,446, doi:10.1029/JA086iA13p11443.

Abdu, M. A., I. S. Batista, and J. H. A. Sobral (1992), A new aspect of magnetic declination control on equatorial spread F and F region dynamo, *J. Geophys. Res.*, *97*(A10), 14,897–14,904, doi:10.1029/92JA00826.

Aquino, M., and V. V. Sreeja (2013), Correlation of scintillation occurrence with interplanetary magnetic field reversals and impact on Global Navigation Satellite System receiver tracking performance, *Space Weather*, *11*, 219–224, doi:10.1002/swe.20047.

Basu, S., and S. Basu (1981), Equatorial scintillations—A review, *J. Atmos. Terr. Phys.*, *43*(5–6), 473–489, doi:10.1016/0021-9169(81)90110-0.

Basu, S., S. Basu, E. MacKenzie, and H. E. Whitney (1985), Morphology of phase and intensity scintillations in the auroral oval and polar cap, *Radio Sci.*, *20*(3), 347–356, doi:10.1029/RS020i003p00347.

Basu, S., E. MacKenzie, and S. Basu (1988), Ionospheric constraints on VHF/UHF communications links during solar maximum and minimum periods, *Radio Sci.*, *23*(3), 363–378, doi:10.1029/RS023i003p00363.

Basu, S., et al. (2001), Ionospheric effects of major magnetic storms during the International Space Weather Period of September and October 1999: GPS observations, VHF/UHF scintillations, and in situ density structures at middle and equatorial latitudes, *J. Geophys. Res.*, *106*(A12), 30,389–30,413, doi:10.1029/2001JA001116.

Beach, T. L. (1998), Global Positioning System studies of equatorial scintillations, PhD thesis, Cornell Univ., Ithaca, New York.

Beach, T. L. (2006), Perils of the GPS phase scintillation index (σ_ϕ), *Radio Sci.*, *41*, RS5S31, doi:10.1029/2005RS003356.

Carrano, C. S., C. E. Valladares, and K. M. Groves (2012), Latitudinal and local time variation of ionospheric turbulence parameters during the Conjugate Point Equatorial Experiment in Brazil, *Int. J. Geophys.*, *2012*, 103963, 16, doi:10.1155/2012/103963.

Carrano, C. S., C. L. Rino, K. M. Groves, and P. H. Doherty (2015), On the mutual coherence function for transionospheric waves and its utility for characterizing ionospheric irregularities with a GNSS scintillation monitor, Proc. 2015 ION Pacific PNT Conference, Honolulu, Hawaii.

Carrano, C. S., K. M. Groves, C. L. Rino, and P. H. Doherty (2016), A technique for inferring zonal irregularity drift from single-station GNSS measurements of intensity (S_4) and phase (σ_ϕ) scintillations, *Radio Sci.*, *51*, 1263–1277, doi:10.1002/2015RS005864.

Conker, R. S., M. B. El-Arini, C. J. Hegarty, and T. Hsiao (2003), Modeling the effects of ionospheric scintillation on GPS/Satellite-Based Augmentation System availability, *Radio Sci.*, *38*(1), 1001, doi:10.1029/2000RS002604.

Costa, E., P. A. Roddy, and J. O. Ballenthin (2014), Statistical analysis of C/NOFS planar Langmuir probe data, *Ann. Geophys.*, *32*, 773–791, doi:10.5194/angeo-32-773-2014.

Dao, E., M. C. Kelley, D. L. Hysell, J. M. Retterer, Y.-J. Su, R. F. Pfaff, P. A. Roddy, and J. O. Ballenthin (2012), On the distribution of ion density depletion along magnetic field lines as deduced using C/NOFS, *Radio Sci.*, *47*, RS3001, doi:10.1029/2011RS004967.

DasGupta, A., S. Ray, A. Paul, P. Banerjee, and A. Bose (2004), Errors in position-fixing by GPS in an environment of strong equatorial scintillations in the Indian zone, *Radio Sci.*, *39*, RS1S30, doi:10.1029/2002RS002822.

de Paula, E. R., F. S. Rodrigues, K. N. Iyer, I. J. Kantor, M. A. Abdu, P. M. Kintner, B. M. Ledvina, and H. Kil (2003), Equatorial anomaly effects on GPS scintillations in Brazil, *Adv. Space Res.*, *31*(3), 749–754, doi:10.1016/S0273-1177(03)00048-6.

de Paula, E. R., O. F. Jonah, A. O. Moraes, E. A. Kherani, B. G. Fejer, M. A. Abdu, M. T. A. H. Muella, I. S. Batista, S. L. G. Dutra, and R. R. Paes (2015), Low-latitude scintillation weakening during sudden stratospheric warming events, *J. Geophys. Res. Space Physics*, *120*, 2212–2221, doi:10.1002/2014JA020731.

de Rezende, L. F. C., E. R. de Paula, I. J. Kantor, and P. M. Kintner (2007), Mapping and survey of plasma bubbles over Brazilian territory, *J. Navig.*, *60*, 69–81, doi:10.1017/S0373463307004006.

Doherty, P. H., S. H. Delay, C. E. Valladares, and J. A. Klobuchar (2003), Ionospheric scintillation effects on GPS in the equatorial and auroral regions, *J. Inst. Navig.*, *50*(4), 235–246.

Forte, B. (2012), Analysis of strong ionospheric scintillation events measured by means of GPS signals at low latitudes during disturbed conditions, *Radio Sci.*, *47*, RS4009, doi:10.1029/2011RS004789.

Forte, B., and S. M. Radicella (2002), Problems in data treatment for ionospheric scintillation measurements, *Radio Sci.*, *37*(6), 1096, doi:10.1029/2001RS002508.

Fremouw, E. J., R. L. Leadabrand, R. C. Livingston, M. D. Cousins, C. L. Rino, B. C. Fair, and R. A. Long (1978), Early results from the DNA Wideband satellite experiment—Complex-signal scintillation, *Radio Sci.*, *13*(1), 167–187, doi:10.1029/RS013i001p00167.

Gwal, A., S. Dubey, R. Wahi, and A. Feliziani (2006), Amplitude and phase scintillation study at Chiang Rai, Thailand, *Adv. Space Res.*, *38*(11), 2361–2365, doi:10.1016/j.asr.2006.02.057.

Haerendel, G. (1973), Theory of equatorial spread F, preprint, Max Planck Inst. Extraterr. Phys., Garching, Germany.

Huang, C.-S., O. de La Beaujardiere, P. A. Roddy, D. E. Hunton, J. Y. Liu, and S. P. Chen (2014), Occurrence probability and amplitude of equatorial ionospheric irregularities associated with plasma bubbles during low and moderate solar activities (2008–2012), *J. Geophys. Res. Space Physics*, *119*, 1186–1199, doi:10.1002/2013JA019212.

Jiao, Y., and Y. T. Morton (2015), Comparison of the effect of high-latitude and equatorial ionospheric scintillation on GPS signals during the maximum of solar cycle 24, *Radio Sci.*, *50*, 886–903, doi:10.1002/2015RS005719.

Jiao, Y., Y. T. Morton, S. Taylor, and W. Pelgrum (2013), Characterization of high-latitude ionospheric scintillation of GPS signals, *Radio Sci.*, *48*, 698–708, doi:10.1002/2013RS005259.

Kelley, M. C., J. J. Makela, O. de La Beaujardière, and J. Retterer (2011), Convective ionospheric storms: A review, *Rev. Geophys.*, *49*, RG2003, doi:10.1029/2010RG000340.

Kil, H., M. DeMajistre, L. J. Paxton, and Y. Zhang (2006), F region Pedersen conductivity deduced using the TIMED/GUVI limb retrievals, *Ann. Geophys.*, *24*, 1311–1316.

Kintner, P. M., H. Kil, T. L. Beach, and E. R. de Paula (2001), Fading timescales associated with GPS signals and potential consequences, *Radio Sci.*, *36*(4), 731–743, doi:10.1029/1999RS002310.

Kintner, P. M., B. M. Ledvina, E. R. de Paula, and I. J. Kantor (2004), Size, shape, orientation, speed, and duration of GPS equatorial anomaly scintillations, *Radio Sci.*, *39*, RS2012, doi:10.1029/2003RS002878.

Kintner, P. M., B. M. Ledvina, and E. R. de Paula (2007), GPS and ionospheric scintillations, *Space Weather*, *5*, S09003, doi:10.1029/2006SW000260.

Li, G., B. Ning, Z. Ren, and L. Hu (2010), Statistics of GPS ionospheric scintillation and irregularities over polar regions at solar minimum, *GPS Solutions*, *14*(4), 331–341, doi:10.1007/s10291-009-0156-x.

Moraes, A. O., F. S. Rodrigues, W. J. Perrella, and E. R. Paula (2012), Analysis of the characteristics of low-latitude GPS amplitude scintillation measured during solar maximum conditions and implications for receiver performance, *Surv. Geophys.*, *33*(5), 1107–1131, doi:10.1007/s10712-011-9161-z.

Moraes, A. O., E. Costa, E. R. de Paula, W. J. Perrella, and J. F. G. Monico (2014), Extended ionospheric amplitude scintillation model for GPS receivers, *Radio Sci.*, *49*, 315–333, doi:10.1002/2013RS005307.

Muella, M. T. A. H., E. R. de Paula, I. J. Kantor, I. S. Batista, J. H. A. Sobral, M. A. Abdu, P. M. Kintner, K. M. Groves, and P. F. Smorigo (2008), GPS L-band scintillations and ionospheric irregularity zonal drifts inferred at equatorial and low-latitude regions, *J. Atmos. Sol. Terr. Phys.*, *70*(10), 1261–1272.

Papoulis, A., and U. Pillai (2002), *Probability, Random Variables, and Stochastic Processes*, 4th ed., McGraw-Hill, New York.

Pi, X., A. J. Mannucci, U. J. Lindqwister, and C. M. Ho (1997), Monitoring of global ionospheric irregularities using the Worldwide GPS Network, *Geophys. Res. Lett.*, *24*(18), 2283–2286, doi:10.1029/97GL02273.

Prikryl, P., P. T. Jayachandran, S. C. Mushini, and R. Chadwick (2011a), Climatology of GPS phase scintillation and HF radar backscatter for the high-latitude ionosphere under solar minimum conditions, *Ann. Geophys.*, *29*, 377–392, doi:10.5194/angeo-29-377-2011.

Prikryl, P., et al. (2011b), Interhemispheric comparison of GPS phase scintillation at high latitudes during the magnetic-cloud-induced geomagnetic storm of 5–7 April 2010, *Ann. Geophys.*, *29*, 2287–2304, doi:10.5194/angeo-29-2287-2011.

Prikryl, P., P. T. Jayachandran, S. C. Mushini, and I. G. Richardson (2014), High-latitude GPS phase scintillation and cycle slips during high-speed solar wind streams and interplanetary coronal mass ejections: A superposed epoch analysis, *Earth Planets Space*, *66*(62), 1–10, doi:10.1186/1880-5981-66-62.

Rodrigues, F. S., M. C. Kelley, P. A. Roddy, D. E. Hunton, R. F. Pfaff, O. de La Beaujardière, and G. S. Bust (2009), C/NOFS observations of intermediate and transitional scale-size equatorial spread F irregularities, *Geophys. Res. Lett.*, *36*, L00C05, doi:10.1029/2009GL038905.

Skone, S., K. Knudsen, and M. de Jong (2001), Limitations in GPS receiver tracking performance under ionospheric scintillation conditions, *Phys. Chem. Earth (A)*, *26*(6–8), 613–621, doi:10.1016/S1464-1895(01)00110-7.

Skone, S., G. Lachapelle, D. Yao, W. Yu, and R. Watson (2005), Investigating the impact of ionospheric scintillation using a GPS software receiver, presented at the ION GNSS 2005 Conference, Long Beach, Calif.

Sobral, J. H. A., M. A. Abdu, H. Takahashi, M. J. Taylor, E. R. de Paula, C. J. Zamlutti, M. G. Aquino, and G. L. Borba (2002), Ionospheric plasma bubble climatology over Brazil based on 22 years (1977–1998) of 630 nm airglow observations, *J. Atmos. Sol. Terr. Phys.*, *64*(12–14), 1517–1524, doi:10.1016/S1364-6826(02)00089-5.

Sreeja, V. V., and M. Aquino (2014), Statistics of ionospheric scintillation occurrence over European high latitudes, *J. Atmos. Sol. Terr. Phys.*, *120*, 96–101, doi:10.1016/j.jastp.2014.09.003.

Sreeja, V. V., et al. (2011), Tackling ionospheric scintillation threat to GNSS in Latin America, *J. Space Weather Space Clim.*, *1*, A05p1–A05p9, doi:10.1051/swsc/2011005.

Su, S.-Y., C. K. Chao, and C. H. Liu (2008), On monthly/seasonal/longitudinal variations of equatorial irregularity occurrences and their relationship with the postsunset vertical drift velocities, *J. Geophys. Res.*, *113*, A05307, doi:10.1029/2007JA012809.

Tsunoda, R. T. (1983), On the generation and growth of equatorial backscatter plumes: 2. Structuring of the west walls of upwellings, *J. Geophys. Res.*, *88*(A6), 4869–4874, doi:10.1029/JA088iA06p04869.

Tsunoda, R. T. (1985), Control of the seasonal and longitudinal occurrence of equatorial scintillations by the longitudinal gradient in integrated E region Pedersen conductivity, *J. Geophys. Res.*, *90*(A1), 447–456, doi:10.1029/JA090iA01p00447.

Tulasi Ram, S., M. Yamamoto, R. T. Tsunoda, S. V. Thampi, and S. Gurubaran (2012), On the application of differential phase measurements to study the zonal large scale wave structure (LSWS) in the ionospheric electron content, *Radio Sci.*, *47*, RS2001, doi:10.1029/2011RS004870.

Van Dierendonck, A. J. (2008), How GPS receivers measure (or should measure) ionospheric scintillation and TEC and how GPS receivers are affected by the ionosphere, paper presented at HMO-UK GPS-Based Workshop, Hermanus Magn. Obs., Hermanus, S. Afr., 2–3 Sep.

Van Dierendonck, A. J., J. Klobuchar, and Q. Hua (1993), Ionospheric scintillation monitoring using commercial single frequency C/A code receivers, paper presented at ION GPS-93, Inst. of Navig., Arlington, Va, Sep.

Vani, B. C., M. H. Shimabukuro, and J. F. G. Monico (2016), Visual exploration and analysis of ionospheric scintillation monitoring data: The ISMR Query Tool, *Comput. Geosci.*, doi:10.1016/j.cageo.2016.08.022, in press.

Xu, R., Z. Liu, M. Li, Y. Morton, and W. Chen (2012), An analysis of low-latitude ionospheric scintillation and its effects on precise point positioning, *J. Global Positioning Syst.*, *11*(1), 22–32, doi:10.5081/jgps.11.1.22.

Yeh, K. C., and C. H. Liu (1982), Radio wave scintillations in the ionosphere, *Proc. IEEE*, *70*(4), 324–360, doi:10.1109/PROC.1982.12313.

Zou, Y., and D. Wang (2009), A study of GPS ionospheric scintillations observed at Guilin, *J. Atmos. Sol. Terr. Phys.*, *71*(17–18), 1948–1958, doi:10.1016/j.jastp.2009.08.005.